Role of microstructure on electrode operating mechanisms for mixed ionic electronic conductors: From synchrotron-based 3D reconstruction to electrochemical modeling

M Hubert, J Laurencin, P Cloetens, Julio Cesar da Silva, F Lefebvre-Joud, P Bleuet, A Nakajo, E Siebert

Role of the Microstructure on Electrode Operating Mechanisms for Mixed Ionic Electronic Conductors: From Synchrotron-Based 3D Reconstruction to Electrochemical Modeling

M. Hubert[a,b,*], J. Laurencin[a], P. Cloetens[b], J.C. da Silva[b],
F. Lefebvre-Joud[a], P. Bleuet[c], A. Nakajo[d], and E. Siebert[e,f]

[a] Univ. Grenoble Alpes – CEA/LITEN, 17 rue des Martyrs, 38054, Grenoble, France
[b] European Synchrotron Radiation Facility (ESRF), 71 avenue des Martyrs, 38000, Grenoble, France
[c] Univ. Grenoble Alpes – CEA/LETI, 17 rue des Martyrs, 38054, Grenoble, France
[d] FUELMAT Group, Faculty of Engineering Sciences (STI), Ecole Polytechnique Fédérale de Lausanne (EPFL), CH-1015 Lausanne, Switzerland.
[e] Univ. Grenoble Alpes – LEPMI, 38000, Grenoble, France
[f] CNRS, LEPMI, 38000 Grenoble, France.

Abstract. A typical $La_{0.6}Sr_{0.4}Co_{0.2}Fe_{0.8}O_{3-\delta}$ (LSCF) electrode was reconstructed by X-ray nanotomography. The new Nano-Imaging beamline ID16A-NI of the ESRF was used to conduct the investigation. Furthermore, a specific attention has been paid to prepare samples with a shape especially well adapted for the tomography experiments, resulting in electrode reconstructions of $51x25.5^2x\pi$ μm^3 with an improved resolution of about 50 nm.

The LSCF microstructural properties were quantified on the 3D volume and used as input data in a dynamic micro-scale electrochemical model. The numerical tool includes two parallel reaction pathways with an oxygen exchange at the LSCF/gas surface and a charge transfer at the electrode triple phase boundaries. Electrochemical impedances were computed in the time domain at open circuit potential, as well as under anodic and cathodic polarizations. Simulations allowed linking the microstructural parameters to the basic mechanisms of electrode operation according to the electrode polarization. A microstructural sensitivity analysis was performed on the single-phase LSCF and LSCF-Ceria doped Gadolinium Oxide (CGO) composite electrodes with the objective to identify the parameters that impact most the electrode response. It was found that the LSCF-CGO composite presents much higher performances compared to the LSCF single phase electrode especially in anodic polarization.

Keywords : SOEC, SOFC, Tomography, Modeling, Impedance spectroscopy, LSCF, LSCF-CGO.

*Corresponding author: Telephone: +33 (0)438782210, Fax: +33 (0)438784139,
E-mail: maxime.hubert@cea.fr

1. Introduction

In the demand of low pollution energy conversion systems, Solid Oxide Cells (SOCs) correspond to promising electrochemical conversion devices operating at high temperatures. Among several advantages, SOCs present a high flexibility in terms of technological applications. Indeed, the same device can be alternatively used in fuel cell and steam electrolysis modes (respectively SOFC and SOEC for Solid Oxide Fuel Cell and Solid Oxide Electrolysis Cell). The SOCs consist in two porous electrodes separated by a dense electrolyte. The usual materials employed for the SOC are Yttria-Stabilized Zirconia (YSZ) for the electrolyte, Ni-YSZ cermet for the H_2 electrode and Mixed Ionic Electronic Conductors (MIECs) such as $La_{0.6}Sr_{0.4}Co_{0.2}Fe_{0.8}O_{3-\delta}$ (LSCF) for the O_2 electrode. In this case, a thin barrier layer of Ceria doped Gadolinium Oxide (CGO) is usually added between LSCF and YSZ to mitigate material reactivity at high temperatures. Moreover, composite electrodes made of LSCF and CGO have been recently proposed to improve the mechanical compatibility with the electrolyte.

The SOCs electrodes have a complex 3D microstructure that plays a major role in the cell electrochemical performances [Virkar,2000, Cai,2011, Lay-Grindler,2013b]. Electrode microstructural properties are also key parameters regarding the cell mechanical robustness [Delette,2013, Liu,2011]. The characterization of the three-dimensional electrodes microstructures is therefore essential to determine morphological properties such as the specific surface area, the tortuosity factor, etc… The implementation of these parameters in electrochemical models allows to unravel the entangled mechanisms of the cell operations and to provide precise guidance for microstructural optimizations.

During the last decade, different 3D characterization methods have been developed to compute the electrodes microstructural properties from a reconstructed volume. Wilson et al. [Wilson,2006] were the first to use a Focused Ion Beam (FIB) coupled with a Scanning Electron Microscope (SEM) to obtain a 3D representation of a SOC electrode. Since this first study, the FIB-SEM technique has been improved to image larger 3D volumes within a reasonable acquisition time [Vivet,2011,Kanno,2011,Joos,2014]. Nowadays, FIB-SEM technique allows the reconstruction of volumes with a typical field of view of 10-15 µm and a spatial resolution of few tens of nanometers (≈10-20 nm) [Vivet,2011, Holzer,2011]. Aside from the FIB-SEM, X-ray tomography techniques constitute other complementary methods to

characterize the microstructure. Among them, transmission X-ray microcopy based on near edge differential absorption has been used by several groups to investigate the microstructure of SOC electrodes [Grew,2010, Cronin,2013, Shearing,2012]. Using X-rays from a synchrotron light source, J.S. Cronin et al. [Cronin,2013] have reported a reconstructed domain with a typical size of ≈40 µm and a spatial resolution announced at 50 nm. Finally, the X-ray holotomography method, which takes advantage of the electron density contrast between the electrode phases, allows obtaining 3D reconstructions with a large field of view of ≈50 µm and an intermediate resolution of ≈75 nm [Villanova,2013]. It can be pointed out that the Representative Volume Element (RVE) of SOC electrodes is proportional to the characteristic length of the microstructure [Harris,2015a, Harris,2015b, Laurencin2012]. Therefore, a reconstructed volume as large as 35x35x35µm^3 is required to obtain good statistics for a Ni-YSZ substrate with a coarse microstructure [Laurencin,2012]; whereas a smaller volume of 13x13x13 µm^3 may be sufficient to describe the fine microstructure of an electrode functional layer [Usseglio-Viretta,2014].

The identification of the relationships between the electrode polarization resistance and microstructural properties measured on 3D reconstruction requires electrochemical models. Several stationary micro-scale models have thus been proposed to link the electrode response to the microstructural parameters for both H_2 and O_2 electrodes [Hajimolana,2011]. However, transient modeling for impedance spectroscopy is a much more powerful tool to understand how the microstructure impacts the basic mechanisms of electrode operation. Nevertheless, in comparison to stationary models, fewer studies have been dedicated to electrochemical impedance simulations as a function of the electrode microstructure [Huang,2007].

Different steady-state models of porous MIEC electrodes operated in SOFC mode have been proposed [Svensson,1997,1998, Coffey,2003,Fleig,2007 ,Carraro,2012, Nicholas,2012, Gong,2014]. Within this frame, the authors have recently developed a stationary model able to simulate the electrochemical response in both SOEC and SOFC modes as a function of the electrode microstructure [Laurencin,2015]. For that purpose, the reactive pathway has been divided into two parallel paths, with a first oxidoreduction at the MIEC/gas surface (bulk path) and a second one at MIEC/gas/CGO Triple Phase Boundaries (TPBs) (surface path). This model was also adapted to simulate the electrochemical behavior for a composite electrode made of LSCF and CGO. Among the most cited electrochemical impedance approaches, Adler, Lane and Steel [Adler,1996] have proposed an analytical solution to calculate impedance spectra for a MIEC single-phase electrode at the Open Circuit Potential

(OCP). The model considers the bulk path with oxygen diffusion in the solid phase and one reaction of oxygen exchange at the MIEC/gas surface. The solution has been derived for boundary conditions representative of a finite-length electrode thickness: on the top of the electrode (at $z=\ell$: see Fig. 3-1), the oxygen flux in the MIEC is equal to the rate of the exchange reaction rate at the surface. They also proposed a simplification for an infinite electrode thickness with a zero oxygen flux when $\ell \to \infty$. This simplified solution is equivalent to a "Gerischer-type" impedance [Boukamp,2003] and is often referred to in other articles as the so-called ALS-model [Nicollet,2015]. Following a similar approach, J.E. Mortensen et al. [Mortensen,2014] have proposed an analytical solution for MIEC-CGO composite electrodes. The model takes into account the oxygen exchange at the MIEC/gas surface and is able to compute impedance diagrams at OCP as a function of the electrode microstructure. The authors have assumed that the oxygen flux in the MIEC is blocked at the top of the electrode layer (i.e. the oxygen flux in the MIEC is considered nil at $z=\ell$ in Fig.3-1). As for the ALS-model, the solution tends to a "Gerisher-type" impedance when the electrode is sufficiently thick ($\ell \to \infty$). Inversely for thin electrodes, the boundary condition leads to restrict the solid-state diffusion resulting in a "finite-length Gerischer-type" impedance with "blocking" condition. In that case, the diagram is constituted by a Gerischer-type element at high frequencies associated to a pure semi-circle at low frequencies. J. Nielsen et al. [Nielsen,2011] have also proposed analytical solutions for the composite electrode. They considered as boundary conditions at $z=\ell$ either a zero oxygen flux or an oxygen concentration in the MIEC fixed at the equilibrium. The first case is equivalent to the approach of J.E Mortensen [Mortensen,2014] while the second case yields a "finite-length Gerischer" impedance (without blocking condition) [Boukamp,2006]. Conversely to the analytical approach, V. Yurkiv et al. [Yurkiv,2014] proposed a pure numerical tool to simulate impedance spectra at OCP with a detailed elementary reaction scheme for the oxygen exchange at MIEC/gas surface. Nevertheless, as for the model proposed by J.E. Mortensen et al. [Mortensen,2014] or J. Nielsen et al. [Nielsen,2011], they did not take into account the plausible charge transfer at the gas/MIEC/CGO TPBs (extended in the whole layer for the MIEC-CGO composite electrode) [Laurencin,2015].

In this work, a typical LSCF electrode has been reconstructed using X-ray holotomography with a large field of view and an improved image spatial resolution. For this purpose, a new sample preparation method has been developed and the experiments were carried out at the

new Nano-Imaging beamline ID16A-NI at the European Synchrotron Radiation Facility (ESRF). A special attention has been paid to estimate the actual resolution in the 3D volume of the reconstructed electrode.

Thanks to the reconstruction, the LSCF microstructural properties were quantified and used as input data in the stationary electrochemical model developed by the authors [Laurencin2015]. In this study, the steady-state model has been extended to compute electrochemical impedance at OCP and under anodic or cathodic polarization. Simulations were performed to determine how the microstructural parameters influence the basic mechanisms of electrode operation as a function of the electrode polarization. Finally, a microstructural sensitivity analysis was performed for the single-phase LSCF and for the LSCF-CGO composite electrodes to identify the parameters that impact most the electrode response.

2. Experimental

2.1 Materials

A sample taken from a symmetrical button cell is analyzed in this work. The cell consists in a dense 260 µm thick electrolyte of 8 mol%Y_2O_3-ZrO_2 (8YSZ) on which two symmetrical electrodes are screen-printed. The two porous layers are made of $La_{0.6}Sr_{0.4}Co_{0.2}Fe_{0.8}O_{3-\delta}$ (LSCF) and are about 25 µm thick. To reduce the detrimental chemical reactivity between LSCF and YSZ, a thin interlayer (2-3µm) of 10%Gd_2O_3-CeO_2 is inserted between the electrolyte and the electrode.

2.1 Sample preparation for X-ray tomography experiments

Adequate sample preparation for the X-ray nanotomography is of central importance for accurate measurements. Both the size and the geometry of the sample impact the quality of the projections recorded during a scan. A thin sample is desirable to limit absorption. In contrast, a sufficiently large volume is necessary to be representative of the main morphological properties of the complete electrode. A complex process involving laser cutting followed by mechanical polishing and wire cutting stage was previously used by the authors [Villanova,2013]. However, the final dimension of the sample was not perfectly controlled. To overcome this issue, sample preparation by milling with Focused Ion Beam (FIB) working

with Gallium is an interesting alternative. Indeed, this equipment is commonly used for the preparation of samples for tomographic measurements. Nevertheless, the drawback is a specimen dimensions restricted to ≈10-20 µm if considering a reasonable process time [Bleuet,2013]. New Plasma-FIBs using Xenon ions allow milling about 60 times faster than a classical Ga-FIB and are therefore promising tools for the preparation of much larger samples [Kwakman,2011]

In this study, the sample has been prepared with a Plasma-FIB Vion (FEI™) using an inductively coupled plasma source of Xe^+ ions. A piece of the cell fixed on a support is placed on a 5-axis motorized stage. Once the vacuum is achieved in the chamber, the first steps consist in the beam focalization and the identification of the eucentric height. This position corresponds to the location where the imaged part of the sample is always the same whatever the rotation and the tilt.

After these preliminary adjustments, a clean and plane zone of interest is chosen at the surface of the electrode. The first step for the preparation is the deposition of a circular platinum protective layer with a thickness of about 2 µm and a diameter close to the required final sample width (Figure 2-1(a)). This layer protects the top of the sample of potential degradation throughout the whole FIB milling process. A sufficiently large ring is initially milled to facilitate the final sample removing by the lift-out process (Figure 2-1(a)). The width and the depth of the FIB milling will have a huge impact on the size of the final sample. This step does not require a high precision and is generally performed using the highest current available on the P-FIB (1.3 µA at 30 kV). Figures 2-1(b) illustrates the FIB milling of the LSCF sample. Several passes are necessary to obtain the final milling depth and to avoid too much sputtered material. The completion of this stage requires about 3-4 hours.
The sample is then removed from the cell and placed on a needle adapted for the tomographic scan. For this step, a micromanipulator located in the P-FIB chamber is used (Figure 2-1(c)). Once fixed on the needle, the diameter of the sample is reduced to the desired value. For this purpose, a low current (59 nA) is selected to obtain a smooth and undamaged surface (Figure 2-1(d)). The produced sample presents a close to perfect axisymmetric geometry which is well adapted for tomographic scan.

2.2 Holotomographic method at the new ID16A beamline

The sample has been characterized by X-ray nanotomography at the ESRF at the new ID16A Nano-Imaging beamline. This new beamline has been designed to achieve high spatial resolution. In that objective, the distance from the X-ray emission source to the position where the sample is analyzed has been increased to 185 m. This specificity of the beamline allows to reach a coherent beam along with a high photon flux. The two high energies available for the experiments are 17.05 keV and 33.6 keV. Thanks to a fixed-angle multilayer optics located at 28 m from the source, a moderate monochromatic beam is obtained with an X-ray bandwidth of about 10^{-2}. The monochromaticity of the beam is limited in order to keep a high photon flux at 185 m. At this position, the X-ray beam is nano-focused by a pair of Kirkpatrick-Baez (KB) mirrors adapted for each beam energy. The mirrors are placed in a large vessel under vacuum that also contains the set-up for the sample nano-positioning. Piezo-motors with a high precision and a good stability are used for the sample positioning and rotation during the tomographic experiments. A high resolution Frelon detector placed behind the vessel records the projections during a scan. It should be noticed that the spatial resolution is bounded by the focal spot size if the stability of the sample and the detector are not limiting. At ID16A, the focal spot size has been evaluated to about 37x23 nm² at 17.05 keV and 21x27 nm² at 33.6 keV.

Several 3D characterization techniques are available at ID16A, such as X-ray fluorescence microscopy or the coherent imaging techniques as ptychography or holotomography. In this study, the LSCF electrode has been reconstructed using holotomography. Phase contrast projections have been recorded using a propagation-based method. As the X-ray beam is nano-focused, magnified projections of the sample are recorded by the detector. The distances between the focal point, the sample and the detector are selected so that the resolution of the magnified projections are independent of the detector pixel size. Projections are obtained at different angles and for different distances between the focal point and the sample to avoid the problem of missing spatial frequencies which can occur for some propagation distances [Zabler,2005].

For the LSCF sample, the beam energy of 17.05 keV was selected for the holotomographic scans. At the 4 different distances between the focus and the sample, each scan consisted in 1500 projections over 180 degrees. For this experiment, the smallest pixel size of 25 nm was

chosen. The exposure time for each projection was 1 second so that about 4 hours were needed to achieve the complete holotomographic scans.

2.3 Three-dimensional reconstruction

The projections saved from the holotomographic scans are a combination of absorption and phase contrast images which are proportional to the electron density of the sample. To reconstruct the 3D volume, a holographic scheme has been used to retrieve the phase [Cloetens,1999, Villanova,2013]. For the phase retrieval, the projections recorded at the four distances from the focal plan are realigned. In addition, all the projections are rescaled down to the smallest pixel dimension recorded during the scan. After this step, a classical tomographic reconstruction is realized by filtered back projection to obtain the final 3D LSCF volume. The procedure for electrode reconstruction has been validated previously for SOC electrode materials in ref. [Quey,2013].

The final LSCF reconstructed electrode presents a field of view of 51.2 μm and a voxel size of 25 nm. A 2D slice extracted from the whole reconstruction is shown in Figure 2-2a. This 3D volume is used to determine the electrode microstructural properties which are essential to simulate accurately the LSCF electrochemical behavior.

3. Electrochemical model description

An in-house model describing MIEC single solid phase and MIEC-CGO composite electrodes was already developed and available for the present study in steady-state operation. This stationary model was presented in details in a previous article [Laurencin, 2015]. In this work, the model has been extended to describe the dynamic behavior of both MIEC single phase and MIEC-CGO composite electrodes. The dynamic model was developed to compute the impedance diagrams at OCP, as well as under anodic or cathodic polarizations. In this section, the main model assumptions regarding the reactive pathway, charge and mass transfers are summarized; whereas the modifications performed to enable transient simulations are more specifically detailed.

As depicted in Fig. 3-1a, the model is isothermal and considers one slice of electrode. In the following description, the model equations are given for the general case of the MIEC-CGO composite bi-material. The limiting case of a single solid phase MIEC electrode is obtained by restricting charge transfer reactions to the interface with the electrolyte ($z=\ell_{CGO}$: see system of coordinate in Fig. 3-1a). These reactions can occur along the Gas/MIEC/CGO Triple Phase Boundaries (TPBs) lengths or across the MIEC/CGO interfaces. Both of these microstructural parameters extend in the depth of the electrode for the composite material but are limited to the interface with the electrolyte in the case of the single phase one.

3.1 Reactive pathway

The reactive mechanism and the expression of the kinetic rates implemented in the model are summarized in Table 1. All the reactions are presented using the 'Kröger-Vink' notation and are expressed in both electrolysis and fuel cell modes (and written in the direction of electrolysis for anodic polarization). In the model, all the forward and backward kinetic constants k_i for each reaction are linked each other by their respective thermodynamic equilibrium constants K_e [Laurencin, 2015]. The proposed reactive pathway is decomposed into a succession of steps that combines a "bulk" and a "surface" path (Fig. 3-1b). Both pathways are joined in a common reaction R4 corresponding the oxygen desorption/adsorption that produces/consumes gaseous oxygen molecules in the electrode porosities.

Table I. Reactive pathways used in the model. Expression of kinetics rates that arise in the electrode thickness (i.e. for $\ell_{CGO} \leq z \leq \ell_{CGO}+\ell$).

Reaction	Expression of the kinetic rate
R1 (bulk path) $2O_o^x(\text{CGO})+2V_o^{\bullet\bullet}(\text{MIEC}) \underset{k_-}{\overset{k_+}{\leftrightarrow}} 2O_o^x(\text{MIEC})+2V_o^{\bullet\bullet}(\text{CGO})$	$v_{(1)} = S_p^{CGO/MIEC}\left\{k_+ \exp\left(\frac{4\alpha_{(1)}^{ox} F E}{RT}\right)\left(1-\frac{C_{O_o^x}}{C_{O_o^x}^{\max}}\right)^2 - k_- \exp\left(-\frac{4\left(\alpha_{(1)}^{red}\right) F E}{RT}\right)\left(\frac{C_{O_o^x}}{C_{O_o^x}^{\max}}\right)^2\right\}$
R2 (bulk path) $2O_o^x(\text{MIEC})+4h^{\bullet}+2s_{MIEC} \underset{k_{red}^{MIEC/Gas}}{\overset{k_{ox}^{MIEC/Gas}}{\leftrightarrow}} 2V_o^{\bullet\bullet}(\text{MIEC})+2O-s_{MIEC}$	$v_{(2)} = S_p^{MIEC/Gas}\left\{k_{ox}^{MIEC/Gas}\Gamma^2\theta_s^2\left(C_{O_o^x}\right)^2 - k_{red}^{MIEC/Gas}\Gamma^2\theta_{O-s}^2\left(C_{O_o^x}^{\max}-C_{O_o^x}\right)^2\right\}$
R3 (surface path) $2O_o^x(\text{CGO})+4h^{\bullet}+2s_{MIEC} \underset{k_{red}^{TPB}}{\overset{k_{ox}^{TPB}}{\leftrightarrow}} 2O-s_{MIEC}+2V_o^{\bullet\bullet}(\text{CGO})$	$v_{(3)} = \xi_{TPB}\left\{k_{ox}^{TPB}\exp\left(\frac{4\alpha_{(2)}^{ox} F E}{RT}\right)\Gamma^2(1-\theta_{O-s})^2 - k_{red}^{TPB}\exp\left(-\frac{4\left(\alpha_{(2)}^{red}\right) F E}{RT}\right)\Gamma^2(\theta_{O-s})^2\right\}$
R4 (common step) $2O-s_{MIEC} \underset{k_{ads}}{\overset{k_{des}}{\leftrightarrow}} O_2(g)+2s_{MIEC}$	$v_{(4)} = S_p^{MIEC/Gas}\left\{k_{des}\Gamma^2\theta_{O-s}^2 - k_{ads}P_{O_2}\Gamma^2\theta_s^2\right\}$

Bulk path — The first step R1 of the bulk path corresponds to the oxygen transfer across the CGO/LSCF interface (Table I) (Fig. 3.1b). In the expressions of the reaction and its kinetic, the term $V_o^{\bullet\bullet}$ represents the oxygen vacancies in the CGO or the MIEC and O_o^x represents the oxygen atoms incorporated in one of the solid phases. The terms k_+ and k_- denote respectively the forward and backward kinetic rate constants for anodic and cathodic polarizations. Although there is no change in the oxidation state between reactants and products, the reaction is still affected by the electrical field arising at the interface between the electrolyte and the MIEC electrode material. For this reason, the reaction rate R1 is expressed by the generalized Butler-Volmer expression. The reaction rate is then computed in the model as a function of the local electrode potential E that corresponds to the electrical field across the CGO/MIEC interface [Laurencin, 2015, Coffey, 2003, Svensson, 1998]. The rate of the reaction R1 is also dependent on the concentration of oxygen atoms incorporated in the MIEC $C_{O_o^x}$. Since the reaction occurs across the interface between CGO and LSCF, its kinetics constants are directly proportional to the MIEC/CGO interfacial specific surface area $S_p^{CGO/MIEC}$.

Once the oxygen is transferred from CGO into the MIEC, it diffuses up to the free surface of electrode particles where it is excorporated into adsorbed oxygen species $O\text{-}s_{MIEC}$ (Fig 3.1b). This second step of the bulk path is described by reaction R2 in Table I and is liable to occur on the whole MIEC/Gas interface. Together with the oxygen transfer from the bulk onto the surface, reaction R2 consumes holes $h^{\bullet}$ and produces an oxygen vacancy $V_o^{\bullet\bullet}$ in the MIEC. As a consequence, the reaction is accompanied with a change in the oxidation state of reactants and products. Nevertheless, R2 is considered in the model as a pure chemical oxidation as discussed extensively in [Laurencin 2015, Svensson, 1997, Adler, 1996, 1998, 2004]. In that condition, its reaction rate is expressed by a classical expression for a pure chemical reaction and depends on (i) the electrode specific surface area $S_p^{MIEC/Gas}$, (ii) the surface density of available sites Γ, (iii) the coverage rate of adsorbed oxygen atoms $\theta_{o\text{-}s}$, (iv)

the concentration of oxygen in the MIEC $C_{O_o^x}$ and (v) the kinetic constants $k_{ox}^{MIEC/Gas}$ and $k_{red}^{MIEC/Gas}$.

As depicted in Fig. 3.1b, the oxygen adsorbates produced on the surface of electrode particles can diffuse and are finally desorbed by reaction R4 (which belongs to the bulk and surface paths).

Surface path — In parallel to the bulk path, the possibility for direct oxidation at the Electrolyte/MIEC/Gas TPBs is included in the model. The reaction mechanism is expressed by R3 and its kinetic rate is computed following the classical generalized Butler-Volmer formalism (table I). In that condition, the rate of the reaction depends on the electrode potential E, the oxygen coverage rate of the electrode surface $\theta_{o\text{-}s}$ and scales linearly with the density of TPBs length ξ_{TPB}.

3.2 Mass and charge transport

The model equations associated to the mass and charge transport are listed in Table II and III. Each equations are briefly described hereafter according to the modelled phases.

Oxygen vacancies diffusion in the MIEC — In electrolysis mode, reaction R2 results in the consumption of oxygen atoms and the production of oxygen vacancies $V_o^{\bullet\bullet}$ at the MIEC/Gas interface. Oxygen vacancies flow toward the CGO/MIEC interface where they are consumed by the ionic transfer R1. The flux of vacancies in the MIEC $N_{V_O^{\bullet\bullet}}$ can be expressed by a solid state diffusion driven by the gradients of chemical and electrical potentials. As MIECs such as LSCF are higher electronic than ionic conductors, it can be demonstrated that the flux of oxygen vacancies follows a classical Fick's law expression [Laurencin, 2015]. The flux is thus proportional to the oxygen vacancy concentration gradient $\nabla C_{V_O^{\bullet\bullet}}$ through the oxygen

chemical vacancy diffusivity $\widetilde{D}_{V_o^{\bullet\bullet}}$. This parameter is expressed with the oxygen vacancy self-diffusion coefficient and the so-called thermodynamic factor [Katsuki, 2003, Elshof, 1997, Laurencin 2015] (Table II). The flux is corrected by the ratio of the volume fraction ε^{MIEC} to the tortuosity factor τ^{MIEC} in order to take into account for the effect of the porous/heterogeneous microstructure of the material on transport [Laurencin, 2015b].

Regarding the equation of oxygen vacancy conservation (Table II), the source terms associated to the kinetic rates of R1 and R2 mean that the flux is modified by the consumption and production of species. Those contributions arise even in the steady-state regime. On the contrary, the temporal term $\varepsilon^{MIEC}\partial C_{V_o^{\bullet\bullet}}/\partial t$ represents the capability of the material to store species on transient periods and consequently depends upon the volume fraction of the MIEC phase.

Migration of holes in the MIEC — The local electronic current density i_{e^-} is linked to the migration of holes in the MIEC. As shown in Table II, the flux is expressed by a classical Ohm's law in which the term $\sigma_{h^\bullet}$ denotes the MIEC electrical conductivity. It is multiplied by the ratio, $\varepsilon^{MIEC}/\tau^{MIEC}$, to accounts for the effect of the electrode microstructure on transport.

In the equation of charge balance (Table II), the faradaic term, $-4F\left(v_{(2)}+v_{(3)}\right)$, is related to the consumption of holes by R2 and R3. The transient component, $S_p^{MIEC/CGO}C_{dl}\partial(\varphi_{MIEC}-\varphi_{CGO})/\partial t$, is ascribed to the capacitance effect of the MIEC/CGO double layer C_{dl}.

Migration of oxygen ions in CGO — In the electrode CGO network (i.e. for $\ell_{CGO} \leq z \leq \ell_{CGO}+\ell$), the ionic current i_{io} obeys the classical Ohm's law. On can note that the intrinsic ionic

conductivity σ_{io} of the material is modified by the microstructural ratio $\varepsilon^{CGO}/\tau^{CGO}$ of the CGO phase. Similarly to the MIEC phase, the charge balance for CGO presents a faradaic contribution induced by the electrochemical reactions R1 and R3. The other contribution is due to the electrode/electrolyte double layer capacitance. It is worth noting that the same value of capacitance has been considered in the model regardless the electrochemical reaction R2 or R3. Indeed, it is assumed that the structure of the double layer depends only on intrinsic properties of materials, and hence, it is the same whatever the position along the MIEC-CGO interface (i.e. in the bulk where R2 happens or in the vicinity of TBBs where R3 occurs).

The pure CGO electrolyte is also considered in the model (i.e. for $0 \leq z < \ell_{CGO:}$ see Fig. 3.1a). It is assumed that the layer is purely resistive and fully dense so that the ionic conductivity corresponds to the material bulk property (table III).

Diffusion of oxygen adsorbates on electrode MIEC surface — The model takes into account surface diffusion of adsorbed oxygen onto the MIEC particles. The associated flux is driven by the gradient in relative coverage of oxygen adsorbates θ_{O-s} as shown in Table II. It is also proportional to (i) the MIEC/Gas specific surface area $S_p^{MIEC/Gas}$, (ii) the density of available site Γ and (iii) the surface diffusivity D_{O-s}. Equation of mass conservation (Table II) is also written in order to take into account the effect of reactions R2 and R3 that produce adsorbed oxygen as well as the reaction R4 that removes the adsorbates from the surface. A dynamic contribution, $S_p^{MIEC/gas}\Gamma\frac{\partial\theta_{O-s}(z,t)}{\partial t}$, is also included in the mass conservation in order to describe the capacity of the surface to store oxygen adsorbates during transient periods.

Gas diffusion in porosity — The electrode gas composition is a mixture of oxygen and nitrogen. Since the pressure gradient remains low in the porosity, the viscous flow is assumed negligible compared to the diffusive flow. Gas phase transport is described by the Dusty Gas Model (DGM) that combines molecular and Knudsen diffusion [Suwanwarangkul,2003]. The effect of the microstructure on gas diffusivities is taken into account by multiplying the

intrinsic properties by the ratio of the volume fraction to the tortuosity factor of the gas phase. The mass conservation is finally written on the oxygen gas flux to describe the variation in gas composition (either due to the desorption reaction R4 or because of transient gas accumulation or depletion in the porosities).

Table II. Model equations for transport, charge and mass conservation in the electrode thickness (i.e. for $\ell_{CGO} \leq z \leq \ell_{CGO}+\ell$).

Process	Equation for transport	Mass or charge conservation
Diffusion of oxygen vacancies in the MIEC	$\vec{N}_{V_O^{\bullet\bullet}}(z) = -\frac{\varepsilon^{MIEC}}{\tau^{MIEC}} \tilde{D}_{V_o^{\bullet\bullet}} \vec{\nabla} C_{V_o^{\bullet\bullet}}$	$\vec{\nabla} \cdot \vec{N}_{V_O^{\bullet\bullet}} = -2v_{(1)} + 2v_{(2)} - \varepsilon^{MIEC} \frac{\partial C_{V_o^{\bullet\bullet}}(z,t)}{\partial t}$
Migration of holes in the MIEC	$\vec{i}_{e^-} = -\frac{\varepsilon^{MIEC}}{\tau^{MIEC}} \sigma_{h^\bullet} \times \vec{\nabla} \varphi_{MIEC}$	$\vec{\nabla} \cdot \vec{i}_{e^-} = -4F\left(v_{(2)} + v_{(3)}\right) + S_p^{MIEC/CGO} C_{dl} \frac{\partial(\varphi_{MIEC} - \varphi_{CGO})}{\partial t}$
Oxygen ionic migration in CGO	$\vec{i}_{io} = -\frac{\varepsilon^{CGO}}{\tau^{CGO}} \sigma_{io} \times \vec{\nabla} \varphi_{CGO}$	$\vec{\nabla} \cdot \vec{i}_{io} = +4F\left(v_{(1)} + v_{(3)}\right) - S_p^{MIEC/CGO} C_{dl} \frac{\partial(\varphi_{MIEC} - \varphi_{CGO})}{\partial t}$
Diffusion of oxygen adsorbates	$N_{O-s} = -S_p^{MIEC/gas} D_{O-s} \Gamma \times \nabla \theta_{O-s}$	$\vec{\nabla} \cdot \vec{N}_{O-s} = +2v_{(2)} + 2v_{(3)} - 2v_{(4)} - S_p^{MIEC/gas} \Gamma \frac{\partial \theta_{O-s}(z,t)}{\partial t}$
Diffusion of gas in electrode porosities	$\frac{dy_{O_2}}{dz} = -\frac{RT}{P_t}\left(\frac{N_{O_2}}{\frac{\varepsilon^{pore}}{\tau^{pore}} D_{k,O_2}} + \frac{y_{N_2} N_{O_2}}{\frac{\varepsilon^{pore}}{\tau^{pore}} D_{O_2,N_2}}\right)$	$\vec{\nabla} \cdot \vec{N}_{O_2} = +v_{(4)} - \frac{\varepsilon^{pore}}{RT} P_t \frac{\partial y_{O_2}(z,t)}{\partial t}$

Table III. Model equations for transport and charge conservation inside the electrolyte thickness (i.e. for $0 \leq z < \ell_{CGO}$).

Process	Equation for transport	Mass or charge conservation
Oxygen ionic migration in CGO	$i_{io} = -\sigma_{io} \times \nabla \varphi_{CGO}$	$\nabla \cdot i_{io} = 0$

3.3 Numerical method

The set of equations has been implemented in the software Comsol® using the integrated mathematical toolbox. The boundary conditions for stationary simulations are detailed in our previous work [Laurencin,2015].

The procedure to compute the transient electrode behavior and more specifically the impedance spectra is summarized hereafter. First, the steady-state model is run at a given overpotential and the stationary solutions are cast as initial values in the related transient

simulation. For the computation of impedance spectra, each point of the diagram is calculated by applying a sinusoidal perturbation to the ionic current density in the electrolyte at z=0:

$$i_{io}(z=0,t) = \bar{i}_{io} + \langle i_{io} \rangle \sin(2\pi f \times t) \quad (1)$$

Where $\bar{i}_{io}$ is the constant ionic current at which the electrode is operated, $\langle i_{io} \rangle$ is the amplitude of the oscillating signal and *f* is the frequency. It is worth noting that the present method is based on the computation of the full nonlinear electrode response. In contrast to the method based on the resolution in the Laplace frequency domain, the present approach does not require any linearization of the oscillating signal [Bessler,2005].

The procedure of data acquisition consist in running simulations for ten full periods, among which the two last are analyzed to estimate the impedance. This method is required to restrict the simulated signal to the steady periodic response [Bessler,2005, Pakalapati,2014]. Moreover, before computing the impedance diagram, a sensitivity analysis has been carried out on the amplitude of the applied signal in the objective to identify the simulating conditions corresponding to the small perturbations assumption. In this work, impedance spectra have been computed in the frequency range 10^{-3}-$5x10^{4}$ Hz by applying an amplitude of $\langle i_{io} \rangle$ =25 mA.cm^{-2}. For each period of the oscillating signal, 1000 values of time are calculated, while up to 70 frequencies are computed for each spectrum.

Finally, the electrode impedance is classically expressed with the transfer function *Z(f)*. One can note that the same impedance spectra are obtained whatever the choice of the applied independent variable (i.e. the ionic current density or the electrode potential). Moreover, for all simulations, it has been checked that the real part of the impedance Real[*Z(f)*] corresponds to the pure resistance of the electrolyte for the highest investigated frequency (i.e. when $f \to \infty$). At the opposite, for the lowest calculated frequency (i.e. $f \to 0$), it has been also verified that Real[Z(f)] is equal to the electrode polarization resistance calculated by the stationary model.

4. Results and discussion

4.1 Resolution of the 3D reconstruction and microstructural quantification

Spatial resolution — The voxel size of the 3D reconstruction is 25 nm but this dimension can differ from the real spatial resolution. Indeed, the number of voxels can be increased without changing the spatial resolution. Thus, it appears necessary to define a way to determine this value. A simple approach for the assessment of the spatial resolution is based on the analysis of the grey level distribution across the boundary between the solid and gas phases. It consists in counting the number of voxels enclosed in the edge between the two phases. Grey scale line profiles have been measured within the electrode 3-D volume in the three space directions for the polar, azimuthal and orthogonal orientations as depicted in Fig. 4-1a to 4-1c. Figure 4-1d shows the grey level distributions as a function of the position across the edge between LSCF and gas. The transition zone contains two voxels of 25 nm for all orientations, which indicates that the spatial resolution of the 3D electrode reconstruction is of almost 50 nm.

This value can be considered as an upper bound for the beam line as the present reconstruction has been obtained with non-optimized parameters for the holotomographic experiments. Indeed, the X-ray beam energy at 17 keV as well as the chosen voxel size are not optimum to achieve the highest image resolution with a SOC sample. Moreover, other relevant methods such as the Fourier Shell Correlation [Van Heel,2005] can be used to refine the assessment of the spatial resolution. This work is out of the scope of the present article and further specific experiments and analysis will be carried out to determine properly this parameter according to tomographic conditions (voxel size, number of projections, etc…).

Microstructural quantification — The 3D volume of the LSCF electrode has been analyzed in order to obtain the main morphological properties. A cubic volume of 22.5x22.5x22.5 μm^3 has been extracted from the whole reconstruction and analyzed with a set of procedures presented in details in [Laurencin,2012, Villanova,2013, Usseglio,2014]. As a summary of the developed workflow, an anisotropic diffusion filter is first applied to improves to separation of the peaks in the grey-level histogram [Villanova,2013]. Then, the volume is segmented with the Otsu method which consists in maximizing the variance between the material phases [Otsu,1979]. After these preliminary steps, the morphological properties as the volume fraction can be determined. The geometric covariogram and its dependent covariance function are used to measure the mean particle diameter and the specific surface area. Finally, the tortuosity factors are calculated with a Finite Element Method (FEM) by determining the effective diffusion coefficient for each phase. All the morphological properties determined on the LSCF electrode are summarized in the Table IV.

The spatial resolution required for the accurate computation of the properties is dependent on the electrode characteristic lengths. By analyzing synthetic microstructure, J.Joos et al. [Joos,2012] has found that around 10-15 voxels on the particle diameter are needed to determine accurately the electrode specific surface area. In the present work, an artificial volume has also been generated using sphere packing and the surface area has been computed using the technique of the geometrical covariogram. It was found that convergence to the theoretical value of S_p is reached at 10 voxels on the particle diameter. Regarding the present characteristic length of the microstructure (0.5 µm: cf. Table IV), the resolution of around 50 nm achieved in the tomographic measurement allows the accurate description of the electrode microstructure.

The minimum size of the Representative Volume Element of the studied electrode has been estimated for the pore volume fraction. Several sub-volumes have been taken from the segmented domain and analyzed. The mean values and the standard deviations are plotted in Fig. 4-2 as a function of the size of the sub-volumes. As expected, the standard deviation decreases by increasing the domain size and becomes equal to σ=0.022 for a length of 7.5 µm. This dimension allows obtaining good statistics and can be considered as the RVE size of the studied electrode. It corresponds to a length of 15 times the mean particle diameter which is consistent with the rule proposed in [Harris,2015a, Harris,2015b, Metcalfe,2010]. Therefore, the fine microstructure of the studied electrode explains the relatively low size of the RVE. Since all the properties have been analyzed on a cube of 22.5 µm, the uncertainty in the computed microstructural parameters should be very low.

As a consequence, all the properties have been determined with a high level of confidence and can be used in the modeling approach. This single phase electrode was used as the reference for the simulations.

Table IV. Microstructural properties calculated on the LSCF reconstructed electrode.

Gas phase	**LSCF phase**

Volume fraction (-)	Tortuosity factor (-)	Mean pore diameter (µm)	Volume fraction (-)	Tortuosity factor (-)	Mean particle diameter (µm)
0.446	1.80	0.5	0.554	1.56	0.46
Interfacial density of TPBs (μm^{-1})		Electrode specific surface area (μm^{-1})		LSCF/electrolyte interfacial surface area (-)	
2.56		3.62		0.55	

4.2 Electrochemical simulations

All the simulations have been carried out at 800°C considering the actual materials of the reconstructed cell (i.e. $La_{0.6}Sr_{0.4}Co_{0.2}Fe_{0.8}O_{3-\delta}$ and $Ce_{0.9}Gd_{0.1}O_{1.95}$: cf. § 2.1). The thermodynamic data, reactions kinetic constants, diffusivities and conductivities are given in [Laurencin,2015]. This set of properties correspond to the input data required for the stationary model. Dynamic simulations require in addition the interfacial capacitance for LSCF/CGO as input parameter. The present analysis considers a value of 5 F/m². Indeed, D. Marinha et al. [Marinha,2012] have characterized by impedance spectroscopy thin films of $La_{0.6}Sr_{0.4}Co_{0.2}Fe_{0.8}O_{3-\delta}$ deposited onto $Ce_{0.9}Gd_{0.1}O_{1.95}$ electrolytes. They found that the semi-circle assigned to the charge transfer at the LSCF/CGO interface presents a capacitance comprised between 1 and 10 F/m². Similarly, Baumann et al. [Baumann,2006] have reported an interfacial capacitance of 6 F/m² for LSCF/CGO samples.

4.2.1 LSCF single-phase electrode

Reference case — The reference case defined for the simulations corresponds to the reconstructed sample (microstructural parameters listed in Table IV, cf. § 4.1).

As experimentally highlighted for LSCF material [Laurencin,2015], the simulated polarization curve (Fig. 4-3a) is asymmetric suggesting a dependence of the reactive mechanism on the polarization. To investigate this possibility, the ratio of kinetic rates between the surface and the bulk paths is shown in Fig. 4-3b. It remains below the unity in cathodic polarization indicating that the reactive pathway is controlled by the bulk path. As discussed and analyzed in [Laurencin, 2015], this result means that in fuel cell mode, the reactive mechanism at T=800°C is decomposed into (i) gas transport in porosities, (ii) oxygen adsorption on the electrode surface, (ii) incorporation into the material, (iii) solid state diffusion in LSCF and (iv) finally ionic transfer into electrolyte (Fig. 3-1b). In electrolysis

mode, the mechanism depends on the range of the electrode polarization [Laurencin,2015]. At low overpotential, the ratio plotted in Fig. 4-3b remains smaller than one because the bulk path still controls the global electrochemical process. At higher polarization, the ratio increases steeply and becomes larger than one. In this case, the reactive pathway is dominated by the surface path, i.e. (i) direct oxidation at TPBs, (ii) surface diffusion onto LSCF particles, (iii) oxygen desorption in porosities and (iv) gas diffusion (Fig. 3-1b).

Impedance spectra have been computed at OCP and in both anodic and cathodic polarizations at i=+/- 0.4 A.cm^{-2} (Fig. 4-4) to analyze in details the rate determining steps for each pathways.

(i) Impedance diagram at OCP: The simulated diagram at OCP shown in Fig. 4-4a exhibits a shape and frequency distribution in qualitative agreement with the experimental spectra reported in [Grunbaum,2006,2009, Liu,2012, , X, Endler-Schuck,2015, Marinha,2012, Adler, 1996, Flura,2015, Ringuedé,2001]. A sensitivity analysis has been performed by varying the reaction kinetic constants and the transport properties to identify each contribution in the spectrum. The analysis has revealed that the semi-circle at low frequencies ($f \leq 1$ Hz) can be ascribed to the surface reactions R2 and R4 related to the adsorption/desorption and incorporation/excorporation steps. Indeed, a decrease of k_{ads} or k_{ox} by 70% clearly increases this contribution at low frequency in the diagram (Fig. 4-4a). Since it corresponds to the largest component of the spectrum, it can be claimed that the surface reactions R2 and R4 constitute the main rate determining steps in the global process at OCP. More precisely, in the simulated conditions, the adsorption/desorption is found to be less limiting than the incorporation/excorporation step (as highlighted by the sensitivity analysis in Fig. 4-4a).

At the opposite side in the diagram, the semi-circle at high frequencies ($f \geq 10^3$ Hz) has been assigned to the charge transfer reactions R1 and R3 arising at the LSCF/CGO interface. Since the reactive pathway at OCP is mainly controlled by the bulk path (Fig. 4-3b), this high frequencies contribution originates from the oxygen ionic transfer R1 through the electrolyte/electrode interface (even if the electrochemical reaction at the TPBs slightly participates to the semi-circle). This attribution of the high frequency semi-circle to the ionic transfer across the LSCF/CGO interface is in good agreement with the identification of physical processes performed on experimental impedance spectra by D. Marinha et al. [Marinha,2012] and by F.S. Baumann et al. [Baumann,2007].

Regarding the contribution distinguished at intermediate frequencies (f≈5-100 Hz), a sensitivity analysis performed on the model transport properties indicates that it is correlated to the bulk oxygen vacancies transport in LSCF. This contribution arises since in the present case of a thin layer of 25 µm, the extent of the reactions is limited by the thickness of the electrode. In others words, the layer affected by the solid-state diffusional process is restricted and bounded by the electrode dimension. Considering a zero flux condition at z=ℓ, this limited diffusion associated to reaction within the porous electrodes leads to the "finite-length" Gerischer-type impedance with "blocking" condition [Mortensen,2014, Nielsen,2011]. Except the high frequency semi-circle due to the charge transfer reaction, it is worth noting that the global shape of the diagram plotted in Fig. 4-4a is consistent with the "finite-length" Gerischer-type impedance with "blocking" condition. This type of impedance has been clearly observed by several authors such as N. Grunbaum et al. [Grunbaum,2006] for LSCF electrodes, A. Ringuedé et al. [Ringuedé,2001] for strontium-doped lanthanum cobaltite (LSC) and even A. Flura et al. [Flura,2015] for over-stoichiometric MIEC. It can be noticed that N. Grunbaum et al. [Grunbaum,2006] and A. Ringuedé et al. [Ringuedé,2001] have fitted their data with an equivalent circuit composed of a Warburg-type impedance at low frequencies in series with a resistance and capacitor element representative of the surface reactions. Nevertheless, as the phenomena are strongly convoluted in the frequency range, the full relevance of this approach could be reviewed using the present modeling tool.

As a conclusion, at OCP and T=800°C for the investigated microstructure and electrode thickness (reference case), it is found that the reactive mechanism is controlled by the bulk path for which the main rate determining steps are the adsorption/desorption and incorporation/excorporation (followed by the solid state diffusion and the ionic transfer trough the CGO/LSCF interface). This set of results is in good agreement with the statements from Adler et al. [Adler,1996] who claimed that "solid state diffusion and O_2 surface exchange dominates the electrochemical behavior" of LSCF.

(ii) Impedance diagram at i=-0.4 A.cm^{-2}: The impedance spectrum simulated under cathodic polarization at i=-0.4 A.cm^{-2} is shown in Fig. 4-4b. In this case, it is reminded that the impedance response is fully controlled by the bulk path (since the ratio of surface to bulk paths tends to zero as shown on Fig. 4-3b).

A first observation is that the semi-circle at high frequencies tends to vanish by increasing the electrode cathodic polarization (Fig. 4-4b). Indeed, this semi-circle has been assigned to the

electrochemical reaction R1, which is activated by the electrode potential. Instead of this contribution, a phase shift of 45° is clearly visible at the highest frequency of the diagram (cf. zoom in Fig. 4-4a). This behavior is related to the well-known Warburg impedance arising at high frequencies in the Gerischer type-element. Unlike the spectrum at OCP, the 45° phase shift at the highest frequencies is thus not convoluted anymore with the contribution of the ionic transfer R1. Finally, the impedance due to the surface reactions of oxygen adsorption and incorporation corresponds to the same low frequency semi-circle as the one attributed at OCP. Indeed, the characteristic frequency of this chemical impedance does not change with the electrode polarization.

(iii) Impedance diagram at $i=+0.4\ A.cm^{-2}$: Under such condition of current density, the cell voltage for the reference case is equal to 0.06 Volts (Fig. 4-3a) and the ratio of the surface to the bulk paths reaches a value of ≈1.85 (Fig. 4-3b). This computed ratio indicates that the reaction R3 at the TPBs prevails over the excorporation step R2. Nevertheless, the contributions of both reactive mechanisms to the overall electrode response remain non negligible. Under this regime, the impedance diagram includes several convoluted processes belonging to both pathways (Fig. 4-4c).

Firstly, the small semi-circle at the highest frequencies ($f \geq 5x10^3$ Hz) corresponds to the charge transfer at the TPBs. Indeed, even if this contribution was very low at OCP, it becomes visible under anodic polarization when the surface paths is promoted. Secondly, the spectrum presents a large flattened "semi-circle" in the intermediate frequency range ($\approx f \approx 5x10^3$-5 Hz). The sensitivity analysis reveals that this contribution is mainly due to the oxygen mass transfer on the surface and in the bulk of the electrode particles. Nevertheless, under this anodic polarization, the diffusion impedance due to the oxygen surface diffusivity is more visible than the one due to the transport of oxygen vacancies in LSCF. In that condition, any change in the diffusion coefficient of oxygen adsorbates $D_{O\text{-}s}$ is found to strongly impact this contribution of the spectrum (Fig. 4-4c). Moreover, in the highest frequency domain of this intermediate contribution, the Warburg impedance is convoluted with the surface reactions of excorporation and desorption. This statement is consistent with the reminiscence of a pure semi-circular contribution observed at the lowest frequencies of the diagram (Fig. 4-4c). It corresponds to the chemical impedance assigned to the surface reactions (mainly controlled in this case by the oxygen desorption R4).

Sensitivity analysis on microstructural properties — The effects of variations in the microstructural properties on the response of the electrode in steady-state and in the frequency domain have been investigated.

(i) Impact of the LSCF tortuosity factor: The LSCF tortuosity factor computed on the reconstructed sample is rather low compared to the data reported for similar electrodes [Lay-Grindler,2013, Joos,2011]. As a consequence, τ^{MIEC} has been multiplied by a factor of three to reach an upper bound regarding SOC electrodes. In that condition, the simulated polarization curve and evolution of the ratio between the surface and the bulk paths are shown by the green dashed lines in Fig. 4-3a and 4-3b. The polarization curve is slightly modified in anodic polarization, compared to the reference case (solid black lines) whereas a non-negligible effect is found in cathodic polarization (Fig. 4-3a). Indeed, the LSCF tortuosity directly influences the oxygen solid-state diffusion, and hence impact the bulk path that governs the electrode operation in fuel cell mode (i.e. cathodic polarization). On the contrary, the surface path which controls the electrode behavior at high anodic overpotential, is not sensitive to the LSCF tortuosity factor. As shown in Fig. 4-3b, the curve of the surface to the bulk paths ratio is slightly shifted towards lower anodic polarization when τ^{MIEC} is increased. This statement means that the passage from the bulk mechanism to the surface one arises at lower overpotential. Indeed, the solid-state diffusion is hindered by increasing τ^{MIEC}, so that the bulk path is disadvantaged to the benefit of the surface path. It can be inferred from the present analysis that the morphological parameter τ^{MIEC} should be tuned to improve the cell performance in fuel cell mode (while the electrode performance is quite insensitive to this parameter in electrolysis mode).

Correspondingly to the steady-state performance, the electrode response in the frequency domain is mainly impacted by the modification of τ^{MIEC} at OCP and under cathodic polarization. Indeed, in these operating conditions, the resistance induced by the oxygen solid-state diffusion in LSCF is significantly increased by increasing τ^{MIEC}. The related contribution

at the intermediate frequencies is then swollen in the impedance diagram and leads to increase the total electrode polarization resistance compared to the reference case (Fig. 4-5a and 4-5b). Moreover, the broadening of the oxygen transport impedance at intermediate frequencies tends to enlarge its convolution with the semi-circle assigned to the surface reactions. As shown in Fig. 4-5a and 4-5b, the result is a larger and flattened "semi-circle" that includes the impedance contributions due to the diffusion process and the surface reactions.

More precisely, the diffusion resistance is exacerbated by decreasing τ^{MIEC} and increasing the current density. That phenomenon tends to restrict the extension of the reactions into the electrode thickness [Cai,2011, Laurencin, 2015b]. In that condition, the characteristic length for diffusion tends to become equal or even lower than the electrode thickness. Therefore, as observed for $3\times\tau^{MIEC}$, the computed diagrams are shifted from a Gerischer-type impedance with "blocking" condition (representative of the reference case) toward a typical Gerischer-type impedance. Indeed, this last element stands for infinite electrode thickness for which the length affected by diffusion is lower than the electrode dimension. It is represented in the Bode plan by a phase shift of 45° followed by a skewed semicircle as observed in Fig. 4-5a and 4-5b for $3\times\tau^{MIEC}$. In other words, these simulated diagrams tend towards the limiting case of a semi-infinite solid-state diffusional process, so that they are approaching the ALS solution [Adler,1996] equivalent to a Gerischer element. It is worth mentioning that, in addition to the "finite-length" Gerischer-type impedance with "blocking" condition, the Gerischer-type response was also successfully employed to interpret the experimental impedance diagrams for MIEC materials [Adler,1996,1998, Endler-Schuck,2015, Nicollet,2015].

This analysis shows that apparent discrepancies in the interpretation of the experimental spectra with a simple Gerischer element or a finite-length Gerischer impedance with blocking condition may stem from differences in electrode microstructure. Indeed, the modeling results clearly indicate that the transition from one case to another strongly depends upon the electrode microstructure.

(ii) Impact of LSCF specific surface area: The specific surface area of the reconstructed sample $S_p^{MIEC/Gas}$ can be considered as a lower bound regarding the published data on LSCF electrodes [Laurencin,2015, Joos,2012]. This morphological parameter has been consequently doubled in the present sensitivity analysis in order to assess its effect on the electrode performance. As shown in Fig. 4-3a, the electrode efficiency is significantly improved over the whole range of investigated polarization. Performances are thus increased in fuel cell mode when the bulk path is predominant, as well as in electrolysis mode when the surface path becomes prevalent. Impedance spectra have been computed at OCP and also under polarizations to unravel the underlying mechanisms of this trend (Fig. 4-6).

As shown on the diagram plotted in Fig. 4-6a, the electrode polarization resistance at OCP is strongly lowered by increasing the specific surface area. Only the low frequencies assigned to the surface reactions are affected by this morphological change. As discussed previously, oxygen adsorption and incorporation are the main limiting steps at OCP. By increasing the surface available for these reactions, the rate of the global process is favored.

The same behavior is observed in cathodic polarization (Fig. 4-6b). However, the decrease of the polarization resistance is less compared to the situation at OCP. It can be also noticed that the relative weight of the contribution due the oxygen bulk diffusion in LSCF is enhanced in the spectrum. Therefore, even if the surface reactions kinetic are improved by increasing $S_p^{MIEC/Gas}$, the oxygen solid-state diffusion under cathodic current limits the rate of the global reactive process.

For the computed diagram in anodic polarization (Fig. 4-6c), the increase of the electrode specific surface area impacts the semi-circle at low frequencies but also contracts the contribution ranging at the medium frequencies. Indeed, for the simulated operating condition (anodic polarization at i=+0.4 A.cm^{-2}), the electrode response is mainly controlled by the surface path for which the oxygen desorption and the surface diffusivities are the two rate determining steps. Since $S_p^{MIEC/Gas}$ affects the reaction kinetic of desorption as well as the flux of oxygen adsorbates (cf. table II), any increase of this parameter lowers their respective impedance in the spectrum.

This analysis identifies the electrode specific surface area as a key parameter for the electrode performance in both electrolysis and fuel cell mode. Further, the underlying mechanisms responsible for the dependence of the electrode performances upon $S_p^{MIEC/Gas}$ change with the operating polarization.

(iii) Other microstructural parameters: The effects of additional morphological and physical properties have been studied in the sensitivity analysis. Among them, the effect of volume fraction and tortuosity factor for the gas phase has been analyzed. In our conditions of simulations, no evolution of the electrochemical performances is found for any "realistic" modification of these microstructure properties. Indeed, as already discussed in [Lay-Grindler, 2013b,], mass transport by gas diffusion is not a limiting step for a porous electrode of few tens of micrometers (25 µm for the present analysis), as long as the gas phase percolates.

In contrast, the LSCF volume fraction ε^{MIEC} has a non-negligible effect on the performance, especially under the regime controlled by the bulk path, i.e., at OCP or under cathodic polarization. For instance, the polarization resistance computed at OCP decreases from ≈0.16 Ω.cm² to ≈0.15 Ω.cm² by increasing the LSCF volume fraction from 0.55 to 0.77. This stems from the direct relationship between the volume fraction of the solid phase and the effective oxygen diffusion coefficient of LSCF (cf. Table II).

When the reactive pathway is shifted toward the surface path under anodic polarization, an impacting parameter could be the number of TPBs at the interface with the electrolyte. Nevertheless, it is found that any increase of the interfacial density of TPBs does not change significantly the electrode performances. This result is explained because the reference electrode already offers a sufficiently high density of interfacial TPBs. In that condition, the electrochemical oxidation at TPBs is not a rate-determining step of the reactive process, which is actually much more limited by the subsequent steps of surface diffusion and oxygen desorption [Laurencin,2015]. Therefore, only an extension of the active TPBs in the depth of the electrode can increase the performances. That microstructure corresponds to a composite LSCF-CGO electrode.

4.2.2 LSCF-CGO composite electrode

The electrochemical behavior of a LSCF-CGO composite architecture has been investigated with the model by a sensitivity analysis performed on the main electrode microstructural properties. In this frame, a reference microstructure has been defined according the parameters listed in table V. They constitute a set of data which are assumed to be representative of a classical composite electrode in terms of volume fractions of each phase [Usseglio-Viretta ,2014, Laurencin,2015b, Joos,2014, Nelson ,2011]. Nevertheless, the selected values for the density of TPBs, tortuosity factors and specific surface area have been chosen such as they range in the lower limits of a typical electrode [Usseglio-Viretta ,2014, Laurencin,2015b, Joos,2014, Nelson ,2011]. They have been thus increased in the sensitivity analysis to assess their impacts on the electrode response.

Table V. Reference microstructure for the LSCF-CGO composite electrode.

CGO volume fraction ε^{CGO} (-)	**LSCF volume fraction** ε^{LSCF} (-)	**Gas volume fraction** ε^{pore} (-)	**CGO/LSCF Interfacial specific surface area** $S_p^{MIEC/CGO}$ (μm^{-1})	**CGO/LSCF Interfacial specific surface area** $S_p^{MIEC/Gas}$ (μm^{-1})
0.35	0.35	0.3	2	3
CGO tortuosity factor τ^{CGO} (-)	**LSCF tortuosity factor** τ^{LSCF} (-)	**Gas tortuosity factor** τ^{pore} (-)	**Density of TPBs** ξ_{TPB} (μm^{-2})	**Mean pore radius** r^{pore} (μm)
1.5	1.5	1.5	0.05	0.25

Reference case — The i-V curve and the ratio of the surface to the bulk path are plotted in Fig. 4-7a and 4-7c. Despite a quite low density of TPBs, it is found that the performance of the simulated composite electrode is higher than the single-phase electrode especially in electrolysis mode. For instance, the current density at +0.03 Volts is increased from +0.173 $A.cm^{-2}$ for the pure LSCF electrode to 0.480 $A.cm^{-2}$ for the LSCF-CGO composite electrode (at -0.03Volts, the current is improved from -0.228 $A.cm^{-2}$ to -0.371 $A.cm^{-2}$). That result is consistent with the experimental study of H.J. Hwang et al. [Hwang,2005] who claimed that "adding CGO to the LSCF electrode resulted in its having a lower polarization resistance than the pure LSCF electrode". The statement is also reported in E.P. Murray et al. [Murray,2002] who measured better performances for the composite electrode than the pure LSCF.

Moreover, as expected for the composite electrode, the ratio of the surface to the bulk path is found to be higher than the unity whatever the investigated overpotential (Fig. 4-7c). This result means that the charge transfer across the LSCF/gas interface is quite negligible compared to the direct oxidoreduction at TPBs. The reactive pathway for the LSCF-CGO composite electrode is thus decomposed into the oxygen solid-state transport, the charge transfer at TPBs, the surface diffusion and the reaction of desorption/adsorption from the LSCF surface. In anodic polarization, the CGO network supports most of oxygen transport function, with only a limited contribution of the LSCF phase. Indeed, in this polarization mode, the fast oxygen ionic transfer R1 compared to the excorporation step R2 results to supply the material in oxygen. The oxygen concentration in LSCF is then increased up to tend to the material saturating value, which, in turn, hindered the oxygen flux [Laurencin,2015]. In cathodic polarization, the participation of LSCF into the oxygen transport is more pronounced since, in this case, the material is not saturated in incorporated oxygen atoms. In fact, LSCF is globally depleted in oxygen due the fast ionic transfer R1 compared to the rate of incorporation R2. One can note that, for this electrode, the gas transfer and the adsorbate diffusion do not limit the whole reactive process [Laurencin,2015].

The impedance spectra computed at OCP and under current are shown in Fig. 4-8. The global shape and frequency distribution is in line with the experimental data reported in [Mortensen,2014] and in [Nielsen,2011] for a "coarse" microstructure.

At OCP and under current, the diagrams indicate a Warburg-type behavior with a frequency line at 45° followed by a transition zone and a semi-circle at low frequencies (Fig. 4-8a). The Warburg impedance is assigned to the oxygen transport in the solid phases of the electrode while the low frequency semi-circle is ascribed to the reaction of adsorption/desorption. Note that a slight deformation of the line at 45° has been detected for the highest investigated frequency range and was attributed to the electrochemical reaction at TPBs.

For the spectrum computed under anodic current (Fig. 4-8c), the contribution due to the oxygen solid-state diffusion is found to be significantly convoluted with the contribution due to due to the reaction of desorption. That results in a 45° line that smoothly turns into a semi-circle. As already discuss for the single-phase electrode, this behavior can be interpreted in term of a Gerischer-type element for a semi-infinite diffusion.

Under cathodic polarization, the contribution due the oxygen adsorption is more marked and results in a rather separate and well-defined semi-circle (comparison of Fig. 4-8b and c). Indeed, the kinetic constant for adsorption is lower than the kinetic for desorption [Laurencin,2015]. In other words, the oxygen desorption in electrolysis mode is easier than the adsorption reaction in fuel cell mode. Therefore, in our conditions, the adsorption step limits the global process in the whole electrode thickness in cathodic polarization. That phenomenon yields to flatten the reaction profile along the electrode thickness, which results in the increase of the characteristic length for the solid-state diffusion. As a consequence, the characteristic length for diffusion tends to become higher than the electrode thickness (Fig. 4-8b). This behavior explains the transition from the Gerischer impedance for the diagram in anodic polarization toward a finite-length Gerischer impedance with blocking condition for the one in cathodic polarization.

Microstructural sensitivity analysis —Impact of the MIEC/gas specific surface area, density of TPBs and tortuosity factors of the solid phases have been studied in the microstructural sensitivity analysis of the composite electrode:

(i) Impact of LSCF/Gas specific surface area: Increasing the specific surface area $S_p^{MIEC/Gas}$ by a factor two improves the global electrode i-V curve (Fig. 4-7a). As shown on the related computed impedance spectra (Fig. 4-8), this microstructural change affects the low frequencies domain of the diagrams related to the reaction of adsorption/desorption. Indeed, the increase in $S_p^{MIEC/Gas}$ results in more active sites for this rate-determining reaction leading to accelerate its kinetic rate, and to lower its contribution in the electrode polarization resistance. This effect is particularly pronounced under cathodic polarization (Fig. 4-7b), since in that condition, the reactive mechanism is specifically controlled by the oxygen adsorption step (as previously discussed, the kinetic for adsorption is lower than that for desorption).

(ii) Impact of density of TPBs: Fig. 4-7 shows that an increase in the density of TPBs from 0.05 μm^{-2} to 0.15 μm^{-2} improves the electrode performance, but the effect is less compared to the variation of $S_p^{MIEC/Gas}$ considered here. This indicates that, in the simulated conditions, the reactive pathway is sensibly more limited by the adsorption/desorption reaction than the oxidoreduction at the triple phases active sites. Any increase in the density of TBPs allows to speed up the reaction rate of the surface reaction leading to reduce its contribution in the impedance diagrams. That phenomenon explains the reduction of the semi-circle ranging in the low frequency region of the impedance spectra when ξ_{TPB} is increased (Fig. 4-8).

(iii) Impact of tortuosity factors of CGO and LSCF: The multiplication of τ^{CGO} by a factor of 4 significantly reduces the electrodes performance especially in anodic polarization (Fig. 4-7a). In contrast, the increase of τ^{MIEC} in the same magnitude than τ^{CGO} affects the performances in cathodic polarization whereas its impact on the i-V curve in anodic polarization is rather limited (Fig. 4-7a).

The trend is confirmed by the impedance spectra computed in electrolysis mode (Fig. 4-9). As shown in the diagrams plotted in Fig. 4-9 under anodic current, the electrode polarization resistance is much more risen by the increase of τ^{CGO} than τ^{MIEC}. Indeed, in this operating mode, it is reminded that oxygen atoms are mainly transferred trough the CGO backbone while the role of LSCF is limited. Therefore, increasing τ^{CGO} decreases the effective oxygen diffusivities in the CGO phase and consequently lower the performance in anodic polarization. In cathodic polarization, the effect of τ^{CGO} and τ^{MIEC} are similar since both solid phases are involved in the oxygen transport.

The simulation results indicate that the electrode i-V curve and impedance spectra are strongly dependent on the electrode microstructure and on the polarization in fuel cell or electrolysis modes. Therefore, studies on these materials require the precise knowledge of the electrode microstructural properties. Moreover, investigations based upon impedance simulations and/or measurements at OCP only conveys partial information for mechanistic studies. Therefore extension of such analysis to conditions under polarization is recommended.

5. Conclusions

A LSCF electrode has been reconstructed by holotomography. A new sample preparation using a specific Xe^+ PFIB equipment has been developed. The high precision and throughput of the device allowed the production of a specimen with a section as large as 50 µm and a controlled axisymmetric geometry, which is well adapted for tomographic measurements.
The nano-holotomographic experiment has been performed at the new Nano-Imaging beamline ID16A at the European Synchrotron Radiation Facility (ESRF). This new beamline has been designed to obtain three-dimensional reconstructions with a combined large field of view and a high spatial resolution. The volume of the reconstructed LSCF electrode material is of $\approx 51 \times 25^2 \times \pi$ µm^3. The spatial resolution has been estimated at ≈50 nm by analysis of the

grey level profile across the interface between the solid and pore phases, which ensures the fine description of the electrode microstructure.

The morphological properties of the electrode have been computed on the reconstructed 3D domain and implemented in a micro-scale model for the simulations of the oxygen reduction/oxidation in the LSCF in both steady-state and transient regimes. Electrochemical impedance simulations have been performed in the time domain by keeping the full non-linearity of the system. Computations have been performed at the Open Circuit Potential (OCP), as well as under anodic and cathodic polarization to analyze the contribution of each mechanistic step in the global reactive process.

At OCP and under cathodic current, the electrode is governed by the bulk path, that is to say the oxygen adsorption and incorporation in the LSCF followed by solid-state diffusion. Under this regime, the impedance spectra computed for the reconstructed electrode exhibits a high frequency contribution assigned to the ionic transfer, a contribution associated to the diffusion of oxygen vacancies in the bulk of the LSCF and a chemical impedance ascribed to the surface reactions of adsorption and incorporation. A finite-length Gerischer element with blocking condition is found representative of the general shape of the computed diagrams at OCP and under cathodic current. This indicates that, for the reconstructed electrode simulated at T=800°C, the characteristic length of diffusion exceeds the electrode thickness.

Under anodic polarization, the reactive pathways is shifted toward the surface path controlled by the direct oxidation at TPBs. Therefore, the impedance spectra under anodic current include several contributions belonging to both pathways. Nevertheless, the diagram presents a large contribution which has been ascribed to the diffusion of oxygen on the surface of the electrode material and in the bulk. The present analysis clearly shows that the combination of precise characterization of the electrode microstructure by 3D imaging with a model capable of simulating impedance diagrams at OCP as well as under polarization, is an efficient tool to unravel the underlying mechanisms of electrode operation.

Finally, the effect of the electrode microstructure on the cell response has been studied by sensitivity analysis for both the single-solid phase LSCF and LSCF-CGO composite electrodes (the reference case corresponding to the reconstructed electrode). The numerical analysis has revealed that some of the morphological properties can have a huge impact on the electrode performances. For the single solid phase electrode, the electrode specific surface area (between MIEC and gas) is found to have a strong impact on the performances in both

cathodic and anodic polarizations. The ratio of the volume fraction to the tortuosity factor for the MIEC phase has a non-negligible impact under cathodic polarization (while its effect is rather negligible under anodic polarization). Moreover, the LSCF-CGO composite presents a much higher performance compared to the LSCF single phase electrode, especially in anodic polarization. In that condition, an electrode made of a LSCF-CGO composite should be particularly relevant for the electrolysis mode.

Electrochemical impedance simulations have allowed the analysis of the reactive mechanisms explaining the dependence of the electrode performances on microstructural properties. For the single solid phase electrode, the underlying mechanisms that explain the dependence of the electrode performance on $S_p^{MIEC/Gas}$ change with the operating polarization. For both electrode types, specific variations in the microstructural properties modify the diagram from a finite-length Gerischer element with blocking condition into a Gerischer-type impedance with semi-infinite diffusion. This explains apparent discrepancies in the analysis of experimental diagrams.

Acknowledgments

The research leading to these results has received funding from the European Union's Seventh Framework Programme (FP7/2007-2013) Fuel Cells and Hydrogen Joint Undertaking (FCH-JU-2013-1) under grant agreement n° 621173 (SOPHIA project) and grant agreement n°621207 (ENDURANCE project). A part of this work has been also obtained in the framework of a national program (DJANGO project) financed by the French National Research Agency (ANR) and OCEAN research programme funded by the CEA.

The authors acknowledge access to the nanocharacterization platform (PFNC) at the Minatec Campus in Grenoble.

References

[Adler, 1996] S.B. Adler, J.A. Lane, B.C.H. Steele, Electrode Kinetics of porous mixed-conducting oxygen electrodes, J. Electrochem. Soc., 143(11) (1996) 3554-3564.

[Adler, 1998] S.B. Adler, Mechanism and kinetics of oxygen reduction on porous $La_{1-x}Sr_xCoO_{3-\delta}$ electrodes, Solid State Ionics, 111, 1998, pp. 125-134.

[Adler, 2004] S.B. Adler, Factors governing oxygen reduction in solid oxide fuel cell cathodes, Chem. Rev., 104 (2004) 4791-4843.

[Baumann,2006] F.S. Baumann, J. Fleig, H.-U. Habermeier, J. Maier, Impedance spectroscopic study on well-defined (La,Sr)(Co,Fe)$O_{3-\delta}$ model electrodes, Solid State Ionics, 177 (2006) 1071–1081.

[Baumann,2007] F.S. Baumann, J. Fleig, G. Cristiani, B. Stuhlhofer, H.-U. Habermeier, J. Maier, Quantitative comparison of mixed conducting SOFC cathode materials by means of thin film model electrode, J. Electrochem. Soc., 154(9) (2007) B931-B941.

[Bessler,2005] W.G. Bessler, A new computational approach for SOFC impedance from detailed electrochemical reaction–diffusion models, Solid State Ionics, 176 (2005) 997-1011.

[Bleuet,2013] P. Bleuet, G. Audoit, J.-P. Barnes, J. Bertheau, Y. Dabin, H. Dansas, J.-M. Fabbri, B. Florin, P. Gergaud, A. Grenier, G. Haberfehlner, E. Lay, J. Laurencin, R. Serra, J. Villanova, Specifications for Hard Condensed Matter Specimens for Three-Dimensional High-Resolution Tomographies, Microsc. Microanal. 19(3) (2013) 726-739.

[Boukamp,2003] B.A. Boukamp, H.J.M. Bouwmeester, Interpretation of the Gerischer impedance in solid state ionics, Solid State Ionics, 157 (2003) 29 – 33.

[Boukamp,2006] B.A. Boukamp, M. Verbraeken, D.H.A. Blank, P. Holtappels, SOFC-anodes, proof for a finite-length type Gerischer impedance?, Solid State Ionics, 177 (2006) 2539–2541.

[Cai,2011] Q. Cai, C.S. Adjiman, N.P. Brandon, Investigation of the active thickness of solid oxide fuel cell electrodes using a 3D microstructure model, Electrochimica Acta, 56 (2011) 10809-10819.

[Cloetens,1999] P. Cloetens, W. Ludwig, J. Baruchel, D. Van Dyck, J. Van Landuyt, J.P. Guigay, M. Schenker, Holotomography : Quantitative phase tomography with micrometer resolution using hard synchrotron radiation x rays, Applied Physics Letters 75 (1999) 2912-2914.

[Carraro,2012] T. Carraro, J. Joos, B. Rüger, A. Weber, E. Ivers-Tiffée, 3D finite element model for reconstructed mixed-conducting cathodes: I. Performance quantification, Electrochimica Acta, 77 (2012) 315-323.

[Coffey, 2003] G.W. Coffey, L.R. Pederson, P.C. Rieke, Competition between bulk and surface pathways in Mixed Ionic and Electronic Conducting Oxygen Electrodes, J. Electrochem. Soc., 150(8) (2003) A1139-A1151.

[Cronin,2013] J.S. Cronin, Y.C.K. Chen-Wiegart, J. Wang, S.A. Barnett, Three-dimensional reconstruction and analysis of an entire solid oxide fuel cell by full-field transmission X-ray microscopy, J. Power sources, 233 (2013) 174-179.

[Delette, 2013] G. Delette, J. Laurencin, F. Usseglio-Viretta, J. Villanova, P. Bleuet, E. Lay, T. Le Bihan, Thermo-Elastic properties of SOFC/SOEC electrode materials determined from three-dimensional microstructural reconstructions, Inter. J. Hydrogen Energy, 38 (2013) 12379-12391.

[Endler-Schuck,2015] C. Endler-Schuck, J. Joos, C. Niedrig, A. Weber, E. Ivers-Tiffée, The chemical oxygen surface exchange and bulk diffusion coefficient determined by impedance spectroscopy of porous $La_{0.58}Sr_{0.4}Co_{0.2}Fe_{0.8}O_{3-\delta}$ (LSCF) cathodes, Solid State Ionics, 269 (2015) 67–79.

[Elshof, 1997] J.E. ten Elshof, M.H.R. Lankhorst, H.J.M. Bouwmeester, Chemical diffusion and oxygen exchange of $La_{0.6}Sr_{0.4}Co_{0.6}Fe_{0.4}O_{3-\delta}$, Solid State Ionics, 99 (1997) 15 – 22.

[Fleig,2007] J. Fleig, R. Merkle, J. Maier, The p(O2) dependence of oxygen surface coverage and exchange current density of mixed conducting oxide electrodes: model considerations, Phys. Chemistry Chemical Phys., 9 (2007) 2713-2723.

[Gong,2014] M. Gong, R.S. Gemmen, D.S. Mebane, K. Gerdes, X. Liu, Simulation of surface-potential driven ORR kinetics on SOFC cathode with parallel reaction pathways, J. Electrochem. Soc., 161(3) (2014) F344-F353.

[Grew,2010] K. N. Grew, Y. S. Chu, J. Yi, A. A. Peracchio, J. R. Izzo, Y. Hwu, F. De Carlo W. K. Chiu, Nondestructive nanoscale 3D elemental mapping and analysis of a solid oxide fuel cell anode, J. Electrochem. Soc., 157(6) (2010) B783-B792.

[Grunbaum,2006] N. Grunbaum, L. Dessemond, J. Fouletier, F. Prado, A. Caneiro, Electrode reaction of $Sr_{1-x}La_xCo_{0.8}Fe_{0.2}O_{3-\delta}$ with x= 0.1 and 0.6 on $Ce_{0.9}Gd_{0.1}O_{1.95}$ at 600≤T≤800 °C, Solid State Ionics 177 (2006) 907–913.

[Grunbaum,2009] N. Grunbaum, L. Dessemond, J. Fouletier, F. Prado, L. Mogni, A. Caneiro, Rate limiting steps of the porous $La_{0.6}Sr_{0.4}Co_{0.8}Fe_{0.2}O_{3-\delta}$ electrode material, Solid State Ionics 180 (2009) 1448–1452.

[Hajimolana,2011] S.A. Hajimolana, M.A. Hussain, W.M.A. Wan Daud, M. Soroush, A. Shamiri, Mathematical modeling of solid oxide fuel cells: A review, Renewable and Sustainable Energy Reviews, 15 (2011) 1893-1917.

[Harris,2015a] W.M. Harris, W.K.S. Chiu, Determining the representative volume element size for three-dimensional microstructural material characterization. Part 1: Predictive models, J. Power Sources, 282 (2015) 552-561.

[Harris,2015b] W.M. Harris, W.K.S. Chiu, Determining the representative volume element size for three-dimensional microstructural material characterization. Part 2: Application to experimental data, J. Power Sources, 282 (2015) 622-629.

[Hildenbrand,2013] N. Hildenbrand, P. Nammensma, D.H.A. Blank, H.J.M. Bouwmeester, B.A. Boukamp, Influence of configuration and microstructure on performance of $La_2NiO_{4+\delta}$ intermediate-temperature solid oxide fuel cells cathodes, J. Power Sources, 238 (2013) 442-453.

[Holzer,2011] L. Holzer, B. Münch, B. Iwanschitz, M. Cantoni, Th. Graule, Quantitative relationships between composition, particle size, triple phase boundary length and surface

area in nickel-cermet anodes for Solid Oxide Fuel Cells, J. Power Sources, 196 (2011) 7076-7089.
[Huang,2007] Q.-A. Huang, R. Hui, B. Wang, J. Zhang, A review of AC impedance modeling and validation in SOFC diagnosis, Electrochimica Acta 52 (2007) 8144–8164.
[Hwang, 2005] H.J. Hwang, J.-W. Moon, S. Lee, E.A. Lee, Electrochemical performance of LSCF-based composite cathodes for intermediate temperature SOFCs, J. Power Sources, 145 (2005) 243-248.
[Joos,2011] J. Joos, T. Carraro, A. Weber, E. Ivers-Tiffée, Reconstruction of porous electrodes by FIB/SEM for detailed microstructure modeling, J. Power Sources, 196 (2011) 7302-7307.
[Joos,2012] J. Joos, M. Ender, T. Carraro, A. Weber, E. Ivers-Tiffée, Representative volume element size for accurate solid oxide fuel cell cathode reconstructions from focused ion beam tomography data, Electrochimica Acta, 82 (2012) 268-276.
[Joos,2014] J. Joos, M. Ender, I. Rotscholl, N.H. Menzler, E. Ivers-Tiffee, Quantification of double-layer Ni/YSZ fuel cell anodes from focused ion beam tomography data, J. Power Sources, 246 (2014) 819–830.
[Kanno,2011] D. Kanno, N. Shikazono, N. Takagi, K. Matsuzaki, N. Kasagi, Evaluation of SOFC anode polarization simulation using three-dimensional microstructures reconstructed by FIB tomography, Electrochimica Acta, 56 (2011) 4015-4021
[Katsuki, 2003] M. Katsuki, S. Wang, M. Dokiya, T. Hashimoto, High temperature properties of $La_{0.6}Sr_{0.4}Co_{0.8}Fe_{0.2}O_{3-\delta}$ oxygen nonstoichiometry and chemical diffusion constant, Solid State Ionics, 156 (2003) 453 – 461.
[Kwakman,2011] L. Kwakman, G. Franz, M.M. Visser Taklo, A. Klumpp, P. Ramm, Characterization and Failure Analysis of 3D Integrated Systems using a novel plasma-FIB system, In FRONTIERS OF CHARACTERIZATION AND METROLOGY FOR NANOELECTRONICS AIP Publishing, 1395(1) (2011) 269-273.
[Laurencin,2012] J. Laurencin, R. Quey, G. Delette, H. Suhonen, P. Cloetens, P. Bleuet, Characterisation of Solid Oxide Fuel Cell Ni-8YSZ substrate by synchrotron X-ray nano-tomography : from 3D reconstruction to microstructure quantification, J. Power Sources, 198 (2012) 182-189.
[Laurencin, 2015] J. Laurencin, M. Hubert, K. Couturier, T. Le Bihan, P. Cloetens, F. Lefebvre-Joud, E. Siebert, Reactive Mechanisms of LSCF Single-Phase and LSCF-CGO Composite Electrodes Operated in Anodic and Cathodic Polarisations, Electrochimica Acta, 174 (2015) 1299-1316.
[Laurencin,2015b] J. Laurencin, J. Mougin, Chapt. 6: High-temperature steam electrolysis, In: Hydrogen Production by Electrolysis, Ed. by A. Godula-Jopek, Wiley, 2015.
[Lay-Grindler, 2013] E. Lay-Grindler, J. Laurencin, J. Villanova, I. Kieffer, F. Usseglio-Viretta, T. Le Bihan, P. Bleuet, A. Mansuy, G. Delette, Degradation Study of the $La_{0.6}Sr_{0.4}Co_{0.2}Fe_{0.8}O_3$ Solid Oxide Electrolysis Cell (SOEC) Anode after High Temperature Electrolysis Operation, ECS Trans., 57(1) (2013) 3177-3187.

[Lay-Grindler, 2013b] E. Lay-Grindler, J. Laurencin, G. Delette, J. Aicart, M. Petitjean, L. Dessemond, Micro-modelling of Solid Oxide Electrolysis Cell: from performance to durability, Int. J. of Hydrogen Energy, 38 (2013) 6917-6929.
[Liu, 2011] X. Liu, C. Martin, , D. Bouvard, S. Di Iorio, J. Laurencin, G. Delette, Strength of highly porous ceramic electrodes, J. Am. Ceram. Soc., 94 (2011) 3500-3508.
[Liu, 2012] M. Liu, D. Ding, K. Blinn, X. Li, L. Nie, M. Liu, Enhanced performance of LSCF cathode through surface modification, Int. J. of Hydrogen Energy, 37 (2012) 8613-8620.
[Marinha,2012] D. Marinha, L. Dessemond, E. Djurado, Electrochemical investigation of oxygen reduction reaction on $La_{0.6}Sr_{0.4}Co_{0.2}Fe_{0.8}O_{3-\delta}$ cathodes deposited by Electrostatic Spray Deposition, J. Power Sources, 197 (2012) 80–87.
[Metcalfe,2010] C. Metcalfe, O. Kesler, T. Rivard, F. Gitzhofer, N. Abatzoglou, Connected three-phase boundary length evaluation in modelled sintered composite solid oxide fuel cell electrodes, J. Electrochemical Soc., 157(9) (2010) B1326-B1335.
[Mortensen,2014] J.E. Mortensen, M. Søgaard, T. Jacobsen, Analytical, 1-Dimensional model of a composite solid oxide fuel cell cathode, J. Electrochem. Soc., 161(3) (2014) F161-F175.
[Murray,2002] E.P. Murray, M.J. Sever, S.A. Barnett, Electrochemical performance of (La,Sr)(Co,Fe)O_3-(Ce,Gd)O_3 composite cathode, Solid State Ionics, 148 (2002) 27-34.
[Nelson ,2011] G.J. Nelson, W.M. Harris, J.J. Lombardo, J.R. Izzo, W.K.S. Chiu, P. Tanasini, M. Cantoni, J. Van Herle, C. Comminellis, J.C. Andrews, Y. Liu, P. Pianetta, Y.S. Chu, Comparison of SOFC cathode microstructure quantified using X-ray nanotomography and focused ion beam-scanning electron microscopy, Electrochemistry communications, 13 (2011) 586-589.
[Nicholas,2012] J.D. Nicholas, L. Wang, A.V. Call, S.A. Barnett, Use of the Simple Infiltrated Microstructure Polarization Loss Estimation (SIMPLE) model to describe the performance of nano-composite solid oxide fuel cell cathodes, Phys. Chemistry Chemical Phys., 14 (2012) 15379-15392.
[Nicollet,2015] C. Nicollet, A. Flura, V. Vibhu, A. Rougier, J.M. Bassat, J.C. Grenier, $La_2NiO_{4+\delta}$ infiltrated into gadolinium doped ceria as novel solid oxide fuel cell cathodes: Electrochemical performance and impedance modelling, J. Power Sources, 294 (2015) 473-482.
[Nielsen,2011] J. Nielsen, T. Jacobsen, M. Wandel, Impedance of porous IT-SOFC LSCF:CGO composite cathodes, Electrochimica Acta, 56 (2011) 7963–7974.
[Otsu,1979] N. Otsu, A threshold selection method from gray-level histograms, IEEE Trans. Syst. Man Cybernetics, SMC 9(1) (1979) 62-66.
[Pakalapati,2014] S. Pakalapati, K. Gerdes, H. Finklea, M. Gong, X. Liu, I. Celik, Micro scale dynamic modeling of LSM/YSZ composite cathodes, Solid State Ionics, 258 (2014) 45–60.
[Quey,2013] R. Quey, H. Suhonen, J. Laurencin, P. Cloetens, P. Bleuet, Direct comparison between X-rat nanotomography and scanning electron microscopy for the microstructure characterization of a solid oxide fuel cell anode, Materials Characterization, 78 (2013) 87-95.

[Ringuedé,2001] A. Ringuedé, J. Fouletier, Oxygen reaction on strontium-doped lanthanum cobaltite dense electrodes at intermediate temperatures, Solid State Ionics, 139 (2001) 167-177.
[Shearing,2012] P.R. Shearing, R.S. Bradley, J. Gelb, F. Tariq, P.J. Withers, N.P. Brandon, Exploring microstructural changes associated with oxidation in Ni-YSZ SOFC electrodes using high resolution X-ray computed tomography, Solid State Ionics, 216 (2012) 69-72.
[Svensson, 1998] A.M. Svensson, S. Sunde, K. Nişancioğlu, Mathematical modeling of oxygen exchange and transport in air-perovskite-yttria stabilised zirconia interface regions, II. Direct exchange of oxygen vacancies, J. Electrochem. Soc., 145(4) (1998) 1390-1400.
[Svensson, 1997] A.M. Svensson, S. Sunde, K. Nişancioğlu, Mathematical modeling of oxygen exchange and transport in air-perovskite-yttria stabilised zirconia interface regions, I. Reduction of intermediately adsorbed oxygen, J. Electrochem. Soc., 144(8) (1997) 2719-2732.
[Suwanwarangkul,2003] R. Suwanwarangkul, E. Croiset, M.W. Fowler, P.L. Douglas, E. Entchev, M.A. Douglas, Performance comparison of Fick's, dusty-gas and Stefan-Maxwell models to predict the concentration overpotential of a SOFC anode, J. Power Sources, 122 (2003) 9-18.
[Usseglio-Viretta ,2014] F. Usseglio-Viretta, J. Laurencin, G. Delette, J. Villanova, P. Cloetens, Quantitative microstructure characterization of a Ni-YSZ bi-layer coupled with simulated cathode polarisation, J. Power Sources, 256 (2014) 394-403.
[Van Heel,2005] M. Van Heel, M. Schatz, Fourier shell correlation threshold criteria, Journal of Structural Biology, 151 (2005) 250-262.
[Villanova,2013] J. Villanova, L. Laurencin, P. Cloetens, P. Bleuet, G. Delette, H. Suhonen, F. Usseglio-Viretta, 3D phase mapping of solid oxide fuel cell YSZ/Ni cermet at the nanoscale by holographic X-ray nanotomography, J. Power Sources, 243 (2013) 841-849.
[Virkar,2000] A.V. Virkar, J. Chen, C.W. Tanner, J.-W. Kim, The role of electrode microstructure on activation and concentration polarizations in solid oxide fuel cells, Solid State Ionics, 131 (2000) 189-98.
[Vivet,2011] N. Vivet, S. Chupin, E. Estrade, T. Piquero, P.L. Pommier, D. Rochais, E. Bruneton, 3D microstructural characterization of a solid oxide fuel cell anode reconstructed by focused ion beam tomography, J. Power Sources, 196 (2011) 7541-7549.
[Wilson,2006] J.R. Wislon, W. Kobsiriphat, R. Mendoza, H.Y. Chen, J.M. Hiller, D.J. Miller, K. Thorton, P.W. Voorhees, S.B. Adler, S.A. Barnett, Three-dimensional reconstruction of a solid-oxide fuel-cell anode, Nature Materials, 5 (2006) 541-544.
[Yurkiv,2014] V. Yurkiv, R. Costa, Z. Ilhan, A. Ansar, W.G. Bessler, Impedance of the surface double layer of LSCF/CGO cathodes: an elementary kinetic model, J. Electrochem. Soc., 161(4) (2014) F480-F492.
[Zabler,2005] S. Zabler, P. Cloetens, J.-P. Guigay, J. Baruchel, M. Schlenker, Optimization of phase contrast imaging using hard X rays, Rev. Sci. Instrum., 76 (2005) 073705-1 073705-7.

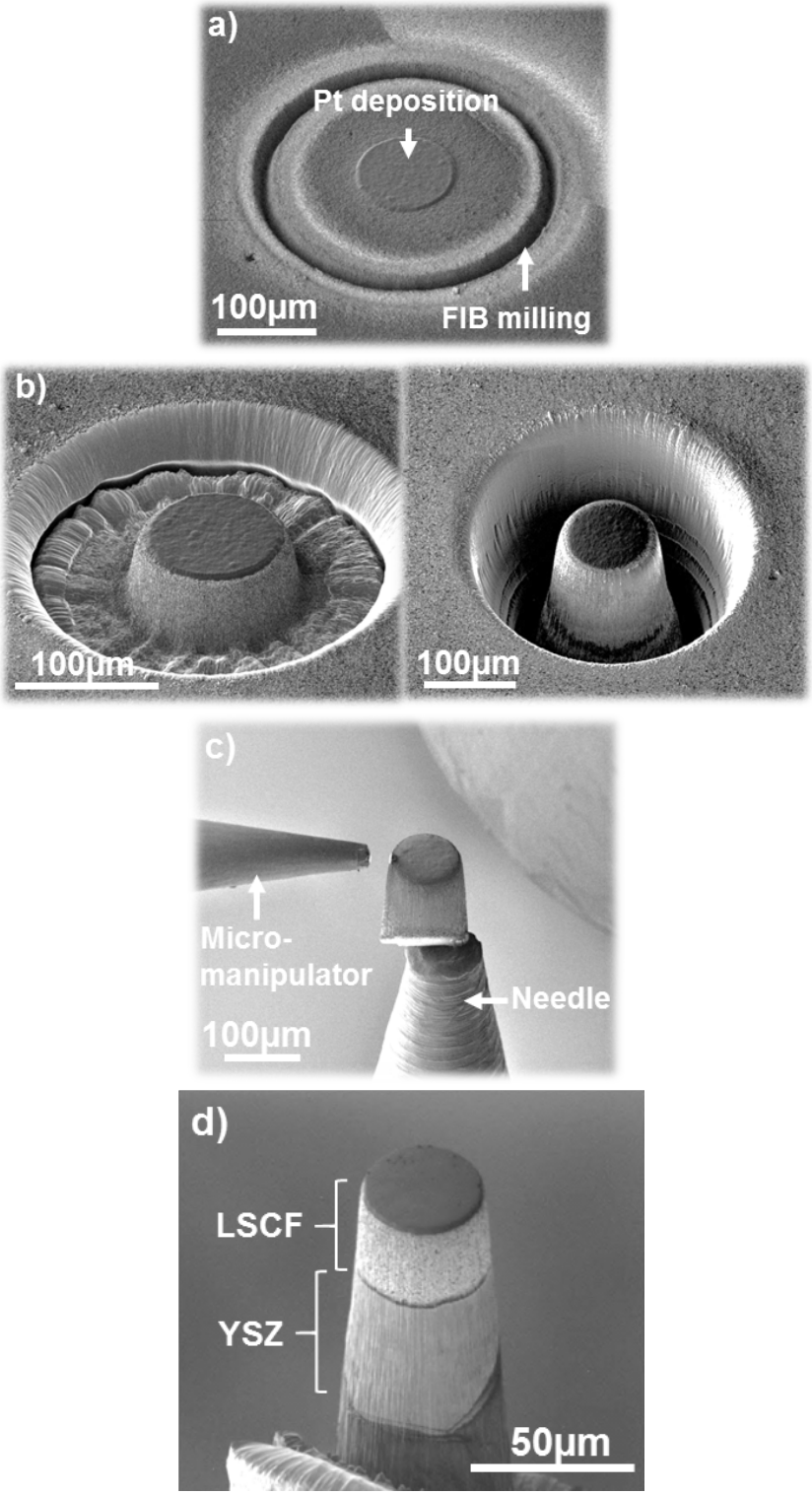

Figure 2-1: Main steps in the sample preparation by FIB : (a) Platinum deposition (b) FIB milling around the sample (c) Lift-out process (d) Sample after the final adjustment of the geometry and cleaning.

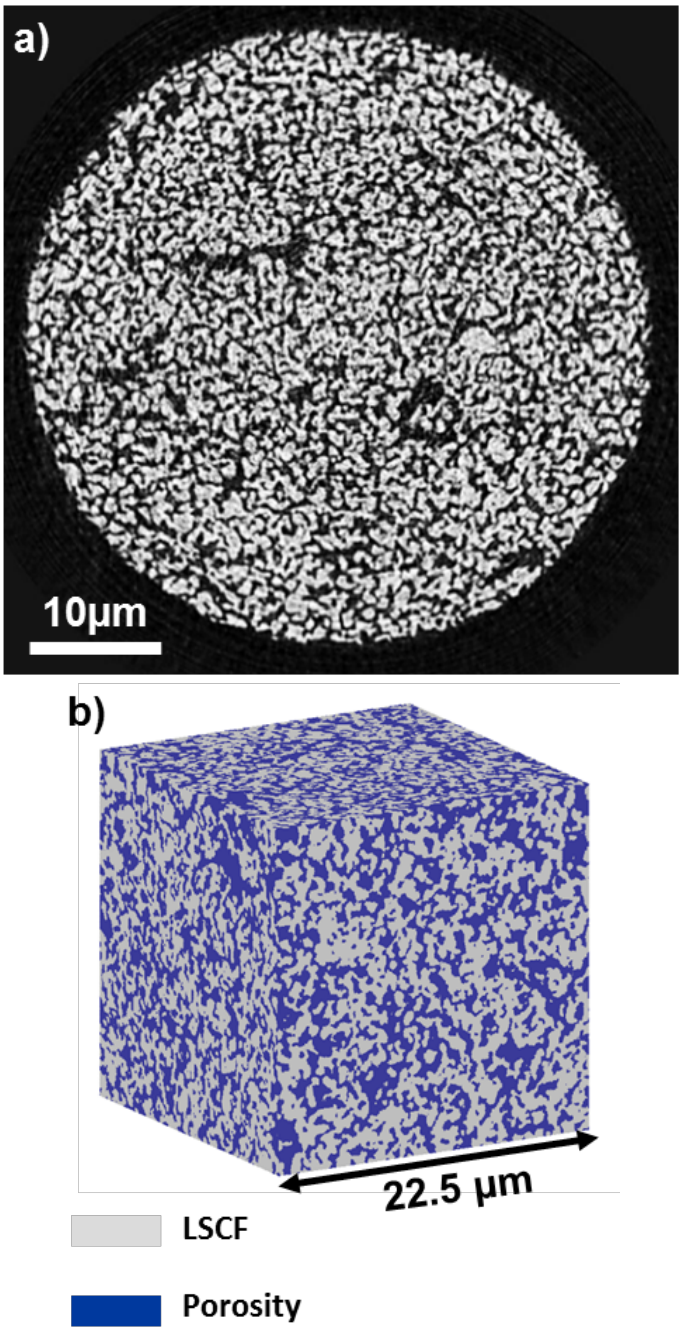

Figure 2-2: (a) Slice extracted from the whole 3D reconstruction of the LSCF sample. The field of view is 51.2 µm and the voxel size is 25 nm. White phase is the LSCF, black phase is porosity. (b) Cubic volume after segmentation and ready for the measurement of the microstructural parameters.

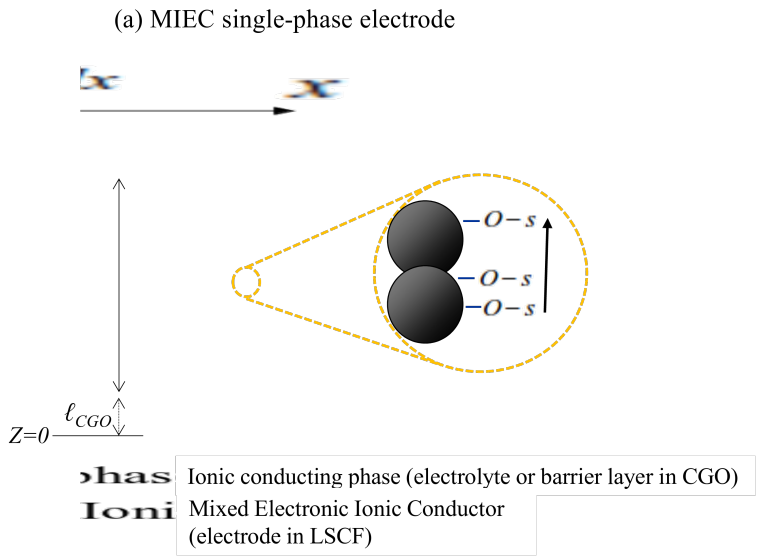

Figure 3-1: (a) Schematic of a single solid phase MIEC electrode in electrolysis mode. The fluxes of oxygen atoms, holes and O_2 gas are represented, with a zoom illustrating the surface diffusion of adsorbed oxygen atoms. (b) A schematic representation of the reactive bulk and surface pathways.

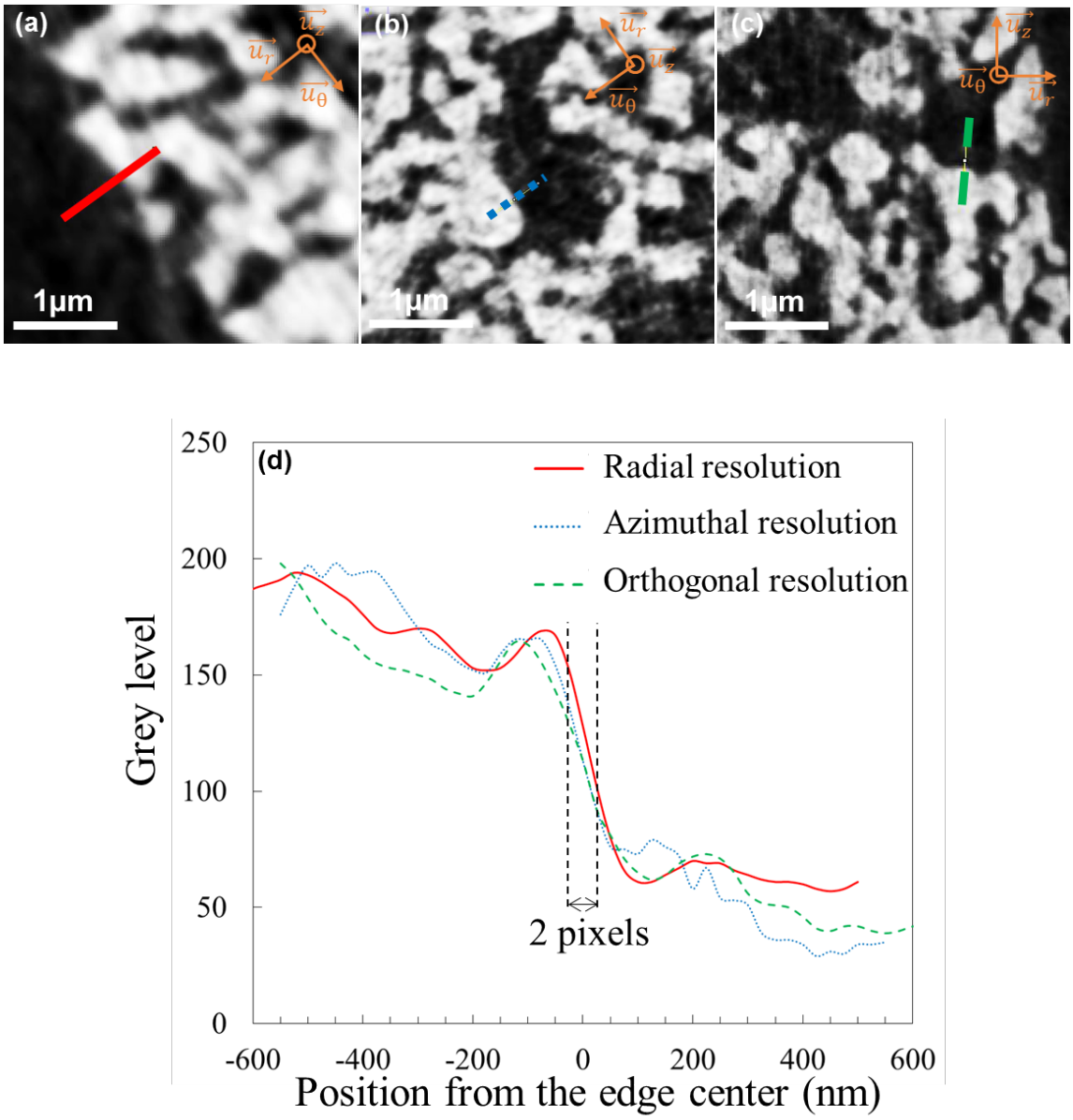

Figure 4-1: Estimation of the resolution: (a) zoom in of the region where the red line profile in d has been plotted for radial resolution, (b) for azimuthal resolution (blue dot line), (c) for orthogonal resolution (green dash line), (d) Grey level plotted as a function of the position in the line profiles. A spatial resolution of about 2 pixels (50 nm) is achieved in the three space directions.

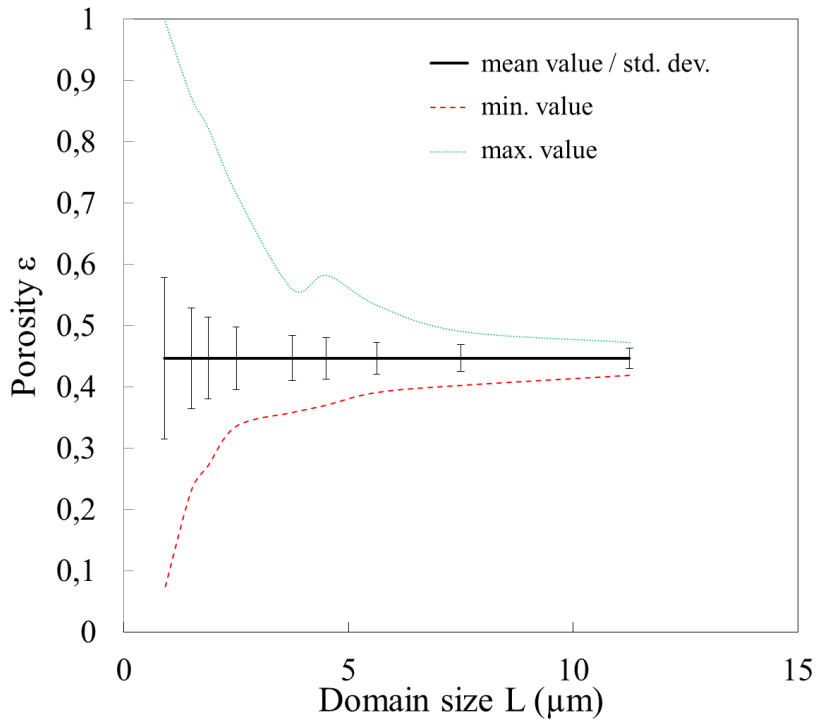

Figure 4-2: Porosity ε plotted as a function of the cube size L^3 extracted from the whole reconstruction to estimate the Representative Volume Element.

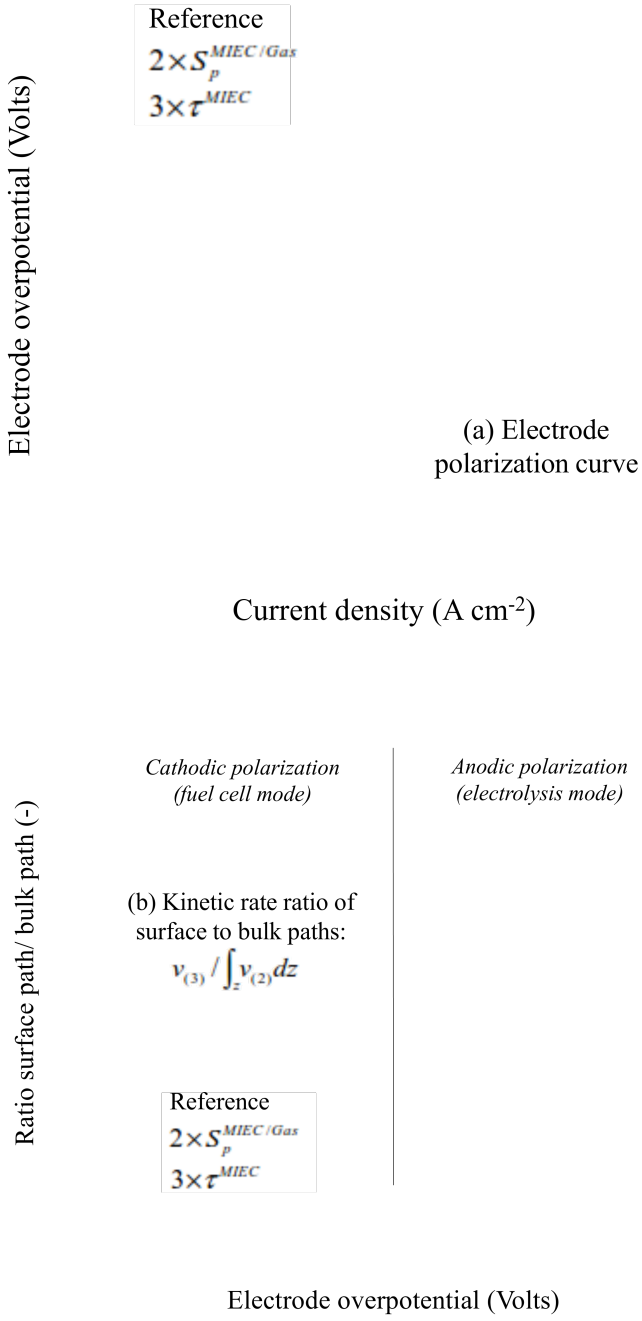

Figure 4-3: (a) Polarization curves for the single solid phase electrode and (b) ratio of kinetic rates between the surface and bulk paths plotted as a function of the electrode overpotential. The solid line corresponds to the reference case (i.e. microstructural parameters listed in table IV and corresponding to the reconstructed electrode). Simulations performed at T=800°C, Po_2=1 atm and for an electrode thickness of 25 µm.

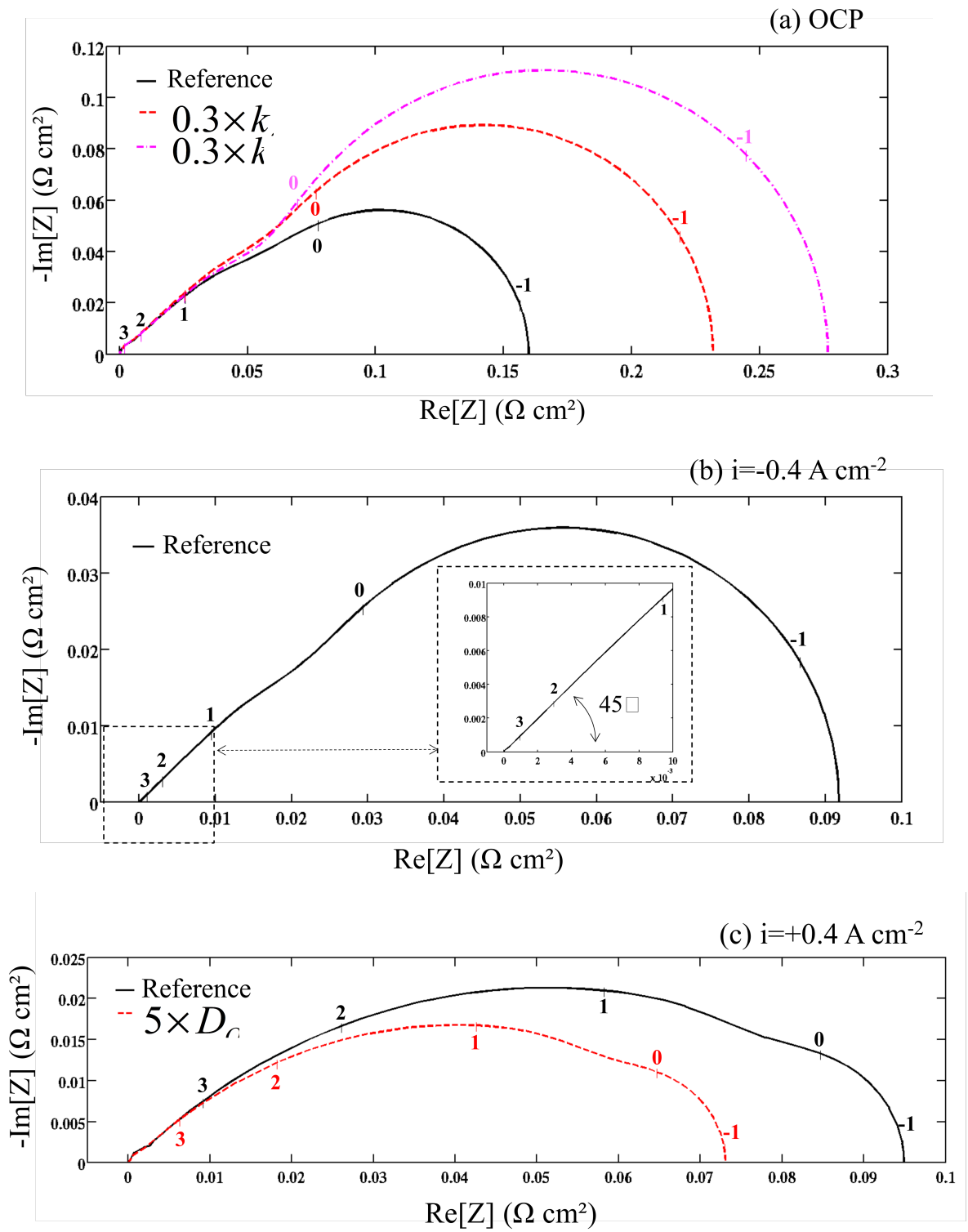

Figure 4-4: Impedance spectra simulated for the single phase electrode (a) at OCP (b) under cathodic current at i=-0.4 A cm^{-2} and (c) under anodic current at i=+0.4 A cm^{-2}. The solid line corresponds to the reference case (i.e. microstructural properties listed in table IV corresponding to the reconstructed electrode). Simulations performed at T=800°C, Po_2=1 atm and for an electrode thickness of 25 µm. The numbers indicates the logarithm of the computed frequency.

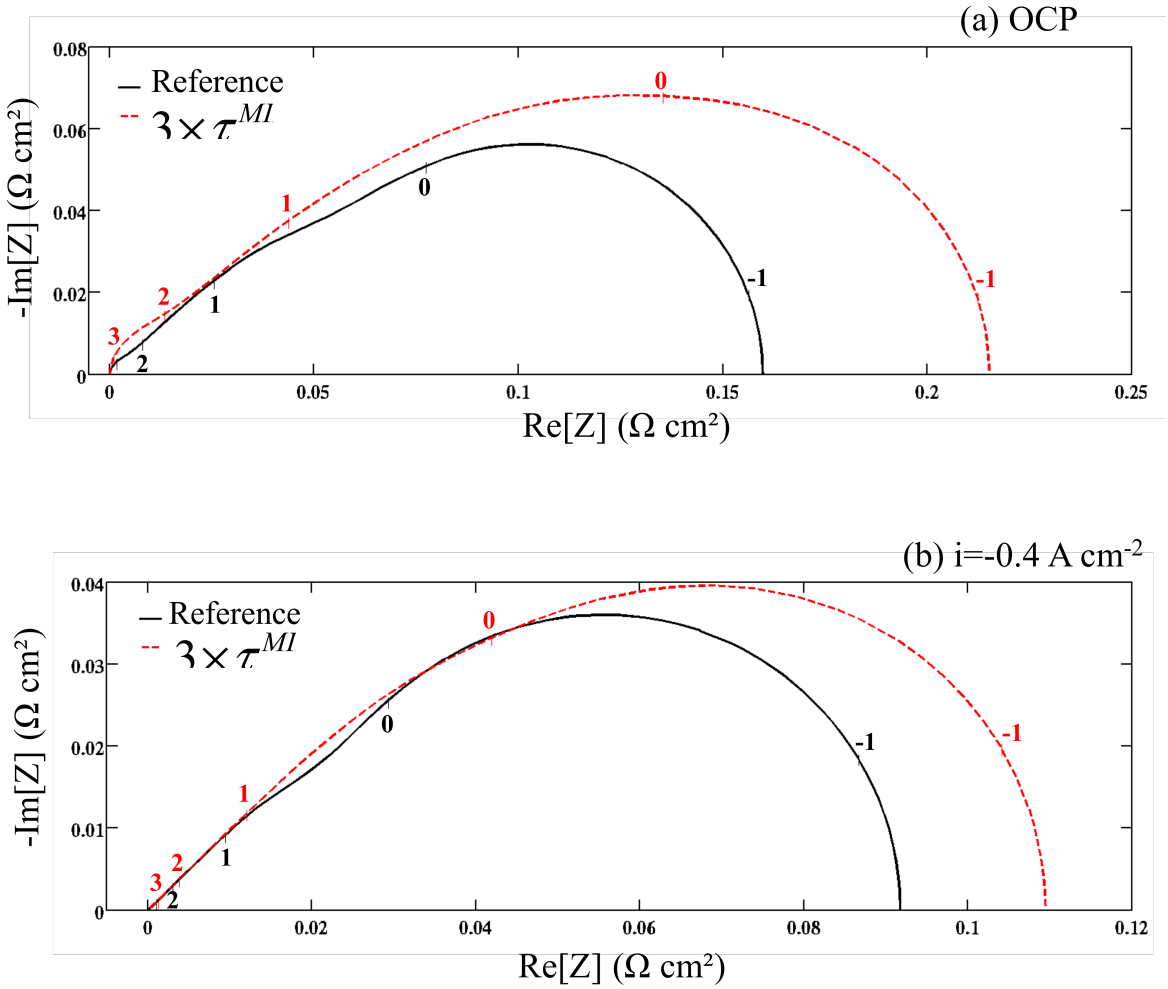

Figure 4-5: Impact of the MIEC tortuosity factor on impedance spectra for the pure LSCF electrode simulated (a) at OCP and (b) under cathodic current at i=-0.4 A cm^{-2}. The solid line corresponds to the reference case (i.e. microstructural properties listed in table IV corresponding to the reconstructed electrode). Simulations performed at T=800°C, Po_2=1 atm and for an electrode thickness of 25 µm. The numbers indicate the logarithm of the computed frequency.

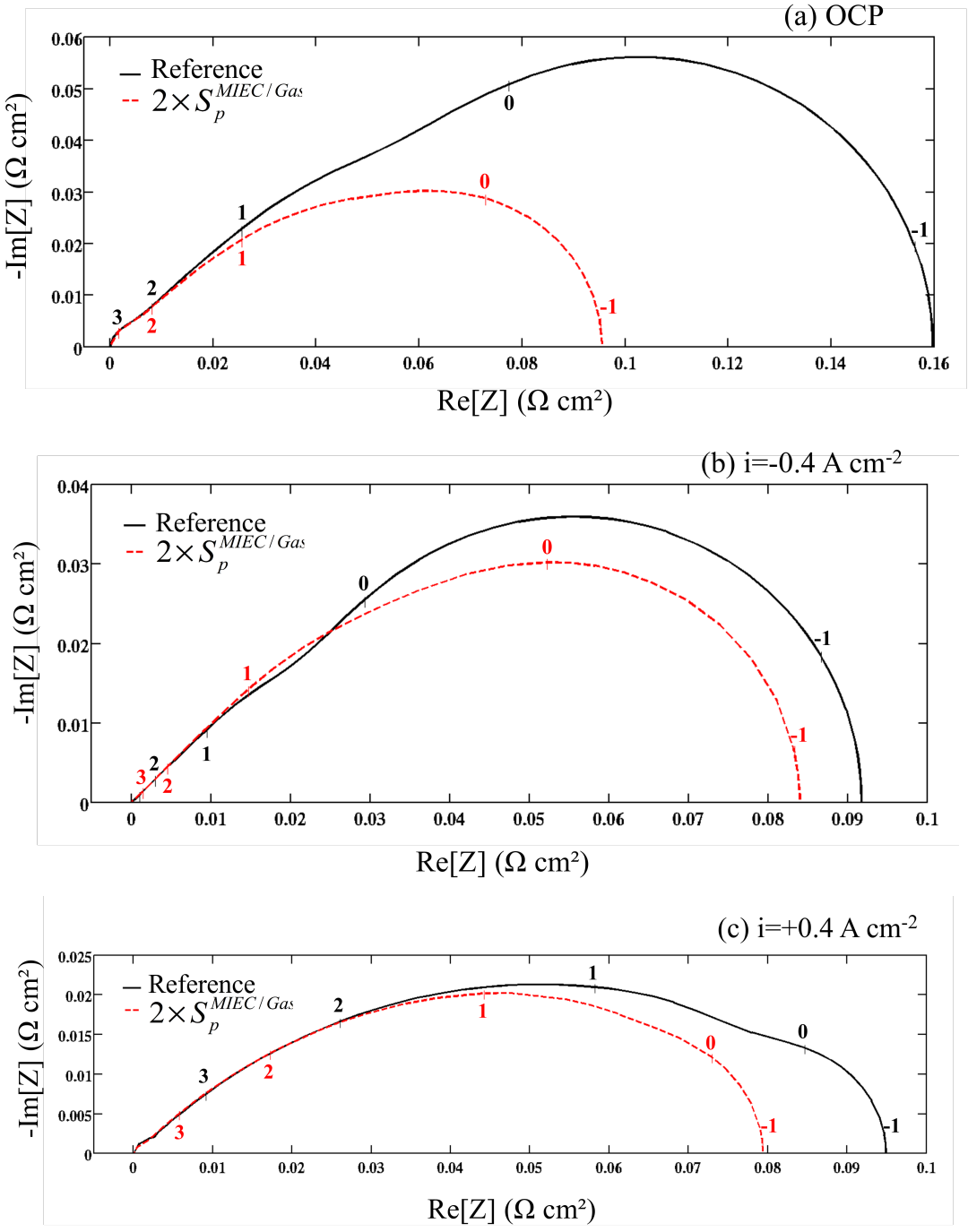

Figure 4-6: Impact of the electrode specific surface area on impedance spectra for the pure LSCF electrode simulated (a) at OCP (b) under cathodic current at i=-0.4 A cm^{-2} and (c) under anodic current at i=+0.4 A cm^{-2}. The solid line corresponds to the reference case (i.e. microstructural properties listed in table IV corresponding to the reconstructed electrode). Simulations performed at T=800°C, Po_2=1 atm and for an electrode thickness of 25 µm. The numbers indicate the logarithm of the computed frequency.

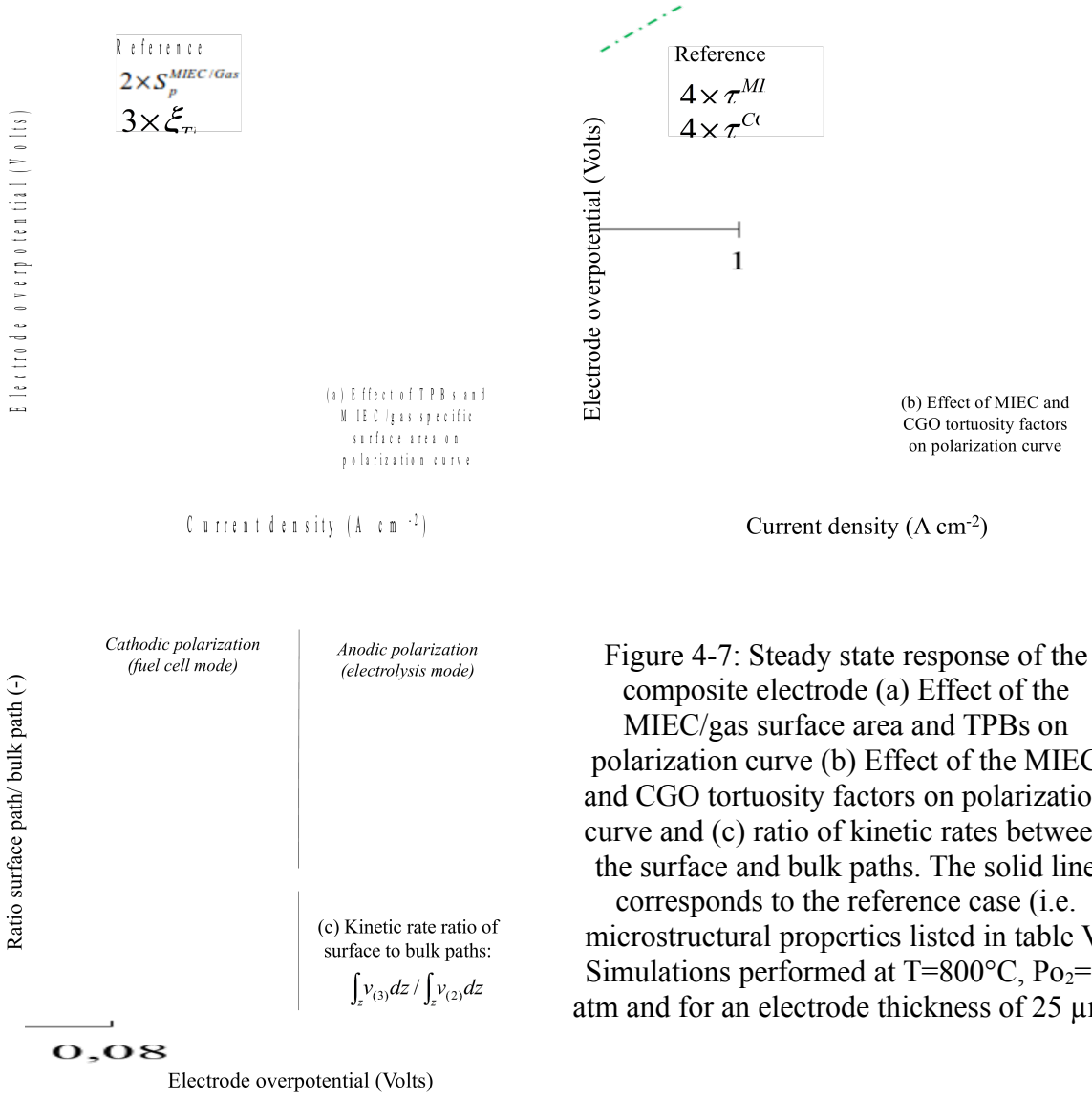

Figure 4-7: Steady state response of the composite electrode (a) Effect of the MIEC/gas surface area and TPBs on polarization curve (b) Effect of the MIEC and CGO tortuosity factors on polarization curve and (c) ratio of kinetic rates between the surface and bulk paths. The solid line corresponds to the reference case (i.e. microstructural properties listed in table V. Simulations performed at T=800°C, Po_2=1 atm and for an electrode thickness of 25 µm.

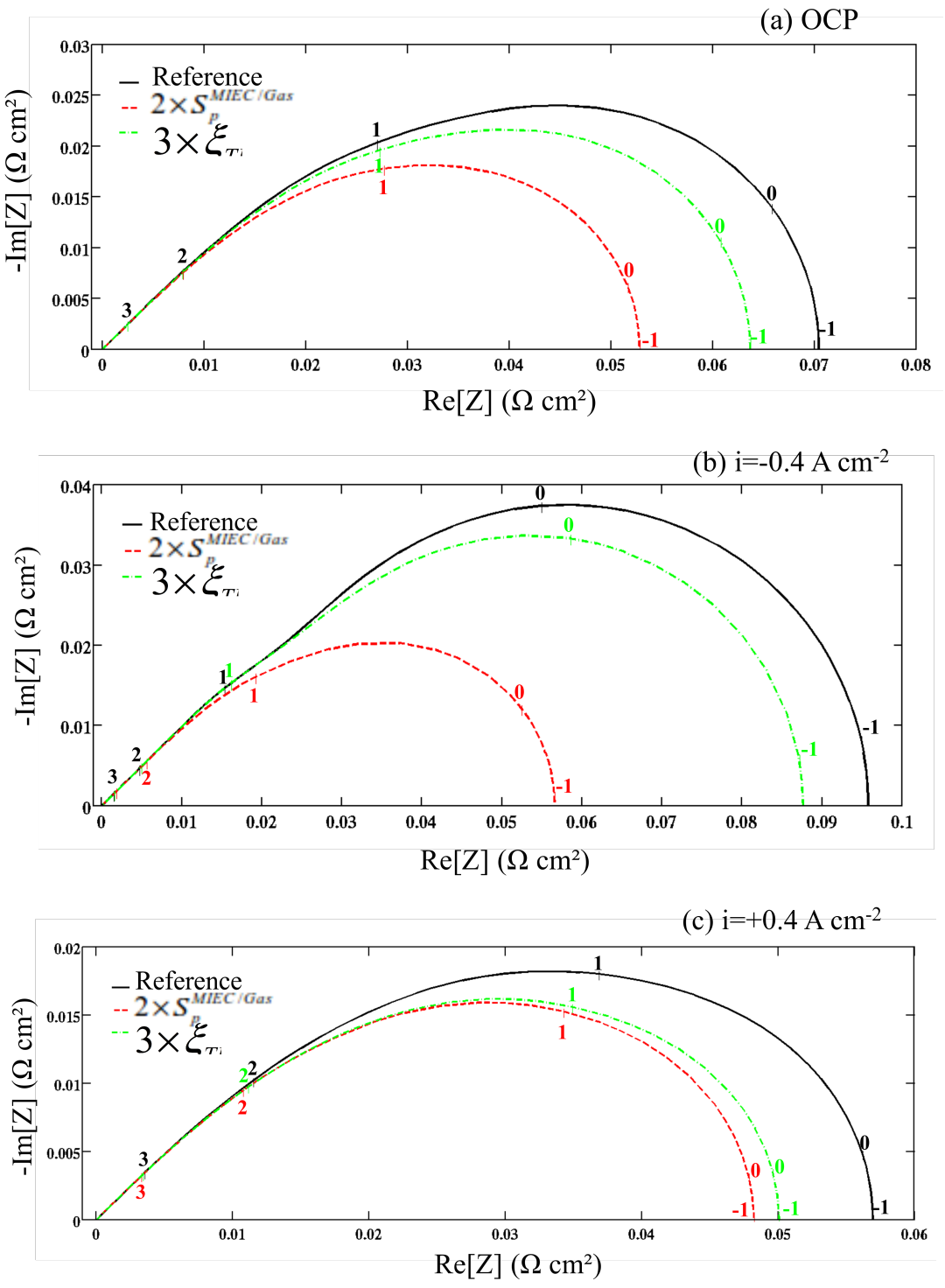

Figure 4-8: Impact of the MIEC/Gas specific surface area and density of TPBs on impedance spectra for the composite electrode simulated (a) at OCP, (b) under cathodic current at i=-0.4 A cm^{-2} and (c) under anodic current at i=+0.4 A cm^{-2}. The solid line corresponds to the reference case (i.e. microstructural properties listed in table V). Simulations performed at T=800°C, Po_2=1 atm and for an electrode thickness of 25 µm. The numbers indicate the logarithm of the computed frequency.

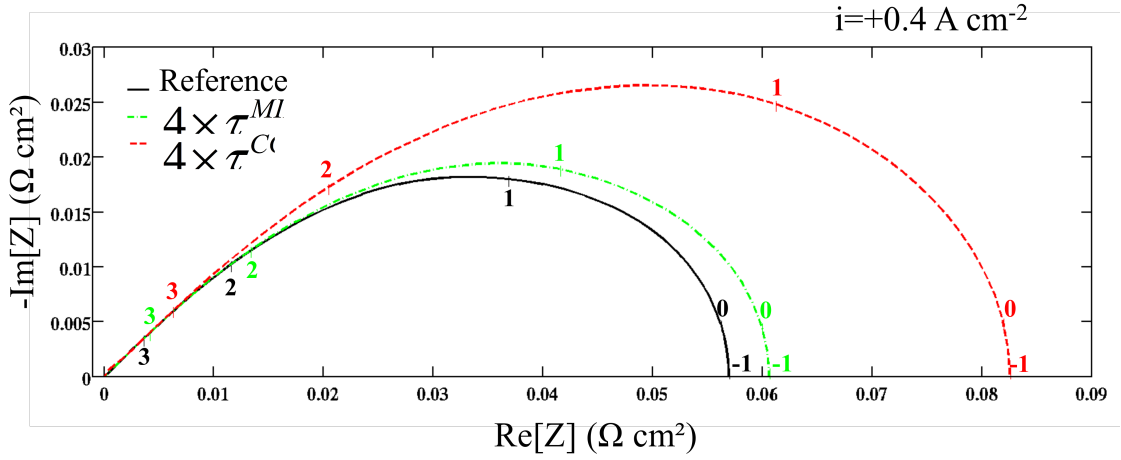

Figure 4-9: Impact of the tortuosity factors of LSCF and CGO on impedance spectra simulated for the composite electrode under anodic current at i=+0.4 A cm^{-2}. The solid line corresponds to the reference case (i.e. microstructural properties listed in table V). Simulations performed at T=800°C, Po_2=1 atm and for an electrode thickness of 25 µm. The numbers indicate the logarithm of the computed frequency.